Kinematics and Kinetics of an In-Parallel-Actuated Soft Manipulator

Olalekan Ogunmolu

***Abstract*—A soft parallel multi-degree of freedom robot is here put forward to counterbalance the heretofore preoccupation with in-parallel rigid robot mechanisms, typically prevalent in frameless and maskless cranial radiation therapy for 6-DOF real-time patient motion correction. Steel-cast or resin-like assembly robot links have their disadvantages particularly in the error magnification at the tool frame owing to the flexure of torques at previous joints, and their uneven load-to-weight ratios. We study the kinematics of our entirely soft robot mechanism using continuum mechanics and differential geometry. We then derive the Newton-Euler system of equations using elasticity theory. Relating the solutions to the boundary value problem of the Cauchy stress for the soft robots links to the force wrenches on the object/load, we write out the manipulation map and construct the associated Jacobian for its direct positioning analysis. Within the bounds here set, the mechanism is intended to provide a minimally-invasive patient motion correction in lieu of the rigid frames and masks in radiation therapy clinics today. Our goal is to edge open the door a little further towards in-parallel soft actuation mechanisms that do not attenuate the radiation beam, are minimally-invasive, and are comfortable for the patient whilst preserving radiation dose and treatment efficacy.**

I. INTRODUCTION

We present the systematic analysis of an in-parallel-actuated soft continuum manipulator for use in clinical radiation therapy. A major application is the real-time closed-loop automatic motion deviation correction, particularly during beam-on time, in robotic radiosurgery; this has the benefits of hastening the current treatment time in clinics, minimizing patient discomfort post-treatment (as opposed to rigid frames and masks currently used in frame and mask-based RT), as well as drastically improving the dose efficacy so that the patient's treatment can be effectively fractionated [1]. It could also find applications in the animation industry where animated plushes are required to be accurately actuated to specific configurations [2], [3]. The real-time control of hyperelastic materials is another possible application [4], [5].

In 2019, an estimated 1,762,450 new cases of cancer was projected to be diagnosed in the United States and 606,880 people was projected to die from the disease. The burden of cancer care is financially significant with estimated national expenditures $147.3 billion [6]. Along with surgery and chemotherapy, radiation therapy (RT) is an essential part of a successful cancer treatment, with more than 50% of all patients receiving RT for the management of their cancers. There have been steady gains in the five-year survival rate for cancer patients, with an improvement of 66% across all cancer types. The increase in survival rate has been attributed in a large part to technological advancements in RT. RT can now tightly conform the radiation dose to the 3D shape of a tumor with approximately 1-2 mm accuracy. This allows for further dose escalation to the tumor, while minimizing dose to nearby healthy organs-at-risk (OAR), and has had significant impact on cancer patients in terms of better tumor control and normal tissue sparing. Unfortunately, RT is currently considered as a static process, whereby treatment plans are calculated based on a snapshot (initial CT scan) of the patient anatomy prior to treatment, and then delivered over the course of a number of weeks. This assumption, that the patients internal anatomy maintains the same position as in the initial CT snapshot over the entire course of treatment is incorrect, and is not compatible with modern RT technology, which can now target radiation dose to the tumor at the millimeter level. Issues involving internal anatomic motion during treatment have become ever more critical to address, and currently limit the potential of modern RT. As an example, for prostate cancer, even with the correct initial patient setup at the linear accelerator (LINAC), the prostate can undergo a wide variety of motions once RT has started, with sudden excursions beyond target in excess of 10mm within a few seconds. As the prostate is located between the bladder and rectum, such motion can lead to incomplete prostate irradiation and undesired irradiation of the bladder, urethra, rectum, erectile tissues, or sphincters – resulting in serious health issues such as incontinence, rectal leakage, or other tissue toxicity [7].

In this work, we derive the kinematics of an evolution of the soft continuum mechanism described in [8] necessary for motion-compensation, as well as planning and control of a patients' H&N motion on a treatment machine. We call the individual soft robots in our mechanism inflatable air bladders (IABs) owing to their hollow internal chambers that admit or release air based on an applied internal pressurization. We derive the manipulator map, kinematics, Jacobian and end-effector velocities. Soft robots are notoriously difficult to control, given their continuum-based mechanical properties, and the inter-dependency of the parameters that characterize their deformation. It is not surprising that different schemes for controlling soft continuum robots have appeared in literature with mixed successes [9]–[15]. For an extensive literature review of the control of continuum soft robots, we refer readers to [16]. The common notations throughout the rest of this

Perelman School of Medicine, The University of Pennsylvania, Philadelphia, PA 19104, USA. Olalekan.Ogunmolu@pennmedicine.upenn.edu

The research reported in this publication was supported by National Cancer Institute of the National Institutes of Health under award number R01CA227124.

©2020 IEEE. Personal use of this material is permitted. Permission from IEEE must be obtained for all other uses, in any current or future media, including reprinting/republishing this material for advertising or promotional purposes, creating new collective works, for resale or redistribution to servers or lists, or reuse of any copyrighted component of this work in other works.

TABLE I: Common Notations in Article

Notation	**Definition**
B	An open set of particles on a Body, B
$\mathscr{B}_\circ$	Closure of the open set of points B in in the reference configuration (arbitrarily chosen) χ_0 over which a non-negative measure of mass is defined.
$\chi(X)$	The motion χ of particles X in $\mathscr{B}$, viz., a one-to-one mapping, from particles, X, of B to their regions in the 3-dimensional Euclidean space $\mathcal{E}$, such that $\chi : B \to \mathcal{E}$ The *place* of particle X in configuration χ is $\boldsymbol{X}$[1].
$X = \chi^{-1}(\boldsymbol{x})$	A region occupied by $\boldsymbol{x}$ (the Euclidean equivalent of $\boldsymbol{X}$) in configuration χ. Essentially, the inverse of the motion $\chi(\cdot)$. [2]
$\mathbf{F}$	The deformation gradient tensor, $\mathbf{F} = \nabla\chi_k(\boldsymbol{X}) = \dot{\chi}_k(\boldsymbol{X})$.
$\boldsymbol{\sigma}$	The Cauchy stress tensor.
$\mathbf{C}$	The right Cauchy-Green Tensor, $\mathbf{C} = \mathbf{F}^T\mathbf{F}$.
$\mathbf{B}$	The left Cauchy-Green Tensor, $\mathbf{B} = \mathbf{F}\mathbf{F}^T$.
$\mathbf{v}(\boldsymbol{x})$	The velocity field $\dot{\chi}(\boldsymbol{x}) = \dot{\chi}(\chi^{-1}(\boldsymbol{X}))$, where without loss of generality, we have taken $X = \boldsymbol{X}$, *i.e.* the place of X.

article are as defined in Table I.

Contributions: We present parallel multi-degree of freedom soft system made out of deformable shells. The individual shells are constrained to strain along the circumferential direction and their kinematic arrangement have actuation freedoms [17] that constraino yield the desired range of motions for the complete manipulation of an object located in their workspace.

- We first provide a constitutive model that governs their deformation given the baked deformation constraints into the material properties of the robots
- We present the type-synthesis of the possible configurations of these soft parallel systems necessary to achieve the full range of motion manipulation of an object in six dimensions
- We analyze the manipulability measure and manipulability ellipsoid for these possible configurations
- We analyze the number- and size- synthesis of the various mechanisms that are achievable with our soft actuation systems
- Lastly, we analyze the kinematics and kinetics of the mechanism with the minimal number of linkages that achieves 6-DOF manipulability.

Iterating from [1], [10], [18]–[21], we expand upon the kinematics and dynamics of the multi-DOF soft actuation system. Our design goals include a system that (1) provides patient comfort whilst manipulating human body parts necessary for trajectory following during RT, (2) assures dose efficacy while not attenuating the ionizing radiation dose treatment due to undesirable material properties (3) capable of emerging complex morphological computational behavior with deformable soft robots – simplifying complex patient motion planning and control during robotic RT treatment.

The rest of this paper is organized as follows: in § III, we review the hardware setup and system configuration, prescribe the finite elastic deformation model and solve the dynamic boundary value problem. We then analyze the contact kinematics with the head in § IV and derive the Newton-Euler Lagrangrian relationship in § V. In § VI, we derive the end-effector velocities and forces; we present manipulation results in § VIII and conclude the paper in § IX. Proofs and derivations are provided in the appendices.

II. Mechanisms Description

We call the individual soft robots in our mechanism inflatable air bladders (IABs) owing to their hollow internal chambers that admit or release air based on an applied internal pressurization.

A. Single Soft Robot Mechanism

Inspired by the papilae of cephalopods (such as octopus and cuttlefish) with respect to their ability to change their perfectly planar and smooth physical texture into a 3D texture up to a specific maximum size [22], we model our soft robots similar to the papilae of these organisms. Here, the elasticity of the soft robot is controlled by a muscular hydrostatic mechanism whereby an elastomeric dermis antagonizes the muscle fibers – causing uniaxial shape erection. We construct the elastic membranes of these soft robots from elastomeric rubber with a shore hardness of 10A (Dragon Skin 10-Medium, Smooth-on Inc.) and control the circumferential strain with nonwoven fabric meshes (Fleishman Fabrics & Supplies, Philadelphia, PA) similar to the design of [23], [24]. Furthermore, inspired by the innervated fins of cuttlefish which allow their mechanoreceptors to process tactile information from their immediate surroundings, we integrate tactile sensorson the outer walls of our soft robots to gather cues for required specific deformations [25]. For this layer, we embed .

vision-based

This internal cavity contributes a single degree of freedom to a soft actuator linkage in the system – in part holding the object in place and moving the it as needed. Each IAB in the closed kinematic chain is linked to the object – each supporting only a part of the total load, redistributing link-loads and solving some of the problems with serial links. Figures 2 - 3 depict the structural characterization of the soft robot mechanism. Inspired by [23], the soft robot chambers are constrained to deform only along the radial strain in order

Fiber or Camera Sensing

layers of sil-

[1]NB: We have dropped the explicit dependence on time due to the final deformation configuration that is of interest to us. Throughout the rest of this paper, we take χ to be a C^2 diffeomorphism.

[2]Note that χ and χ^{-1} are continuous functions of their argument.

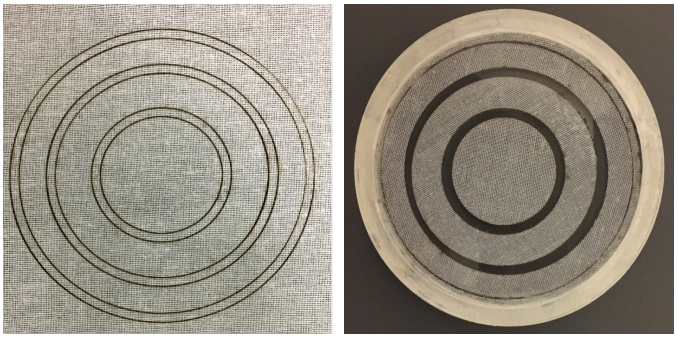

Fig. 1: Fabrication of the soft robot. **Left**: A non-woven fabric is laser-cut in concentric circular patterns. **Right**: Uncured silicone with equal parts of Dragon Skin 10M A and B) with the fabric membrane laid on it (the cuts have been removed). The admixture is allowed to cure at room temperature, under vacuum degassification at 29in Hg before demolding. We then post-cured the admixture at $176°F$ for 2 hours and $212°F$ for 1 hour respectively in order to allow the rubber material to attain its maximum physical properties.

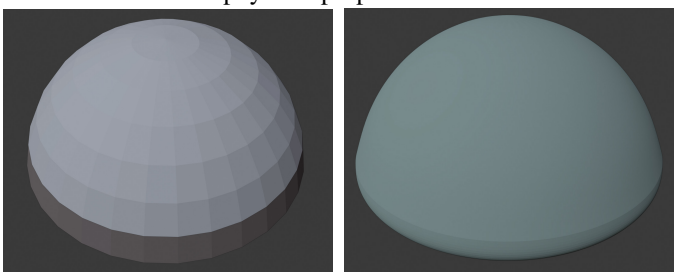

Fig. 2: **Left**: Computer animation of the discrete layers of soft robot at full inflation. **Right**: Gaussian curvature of IABs upon full inflation.

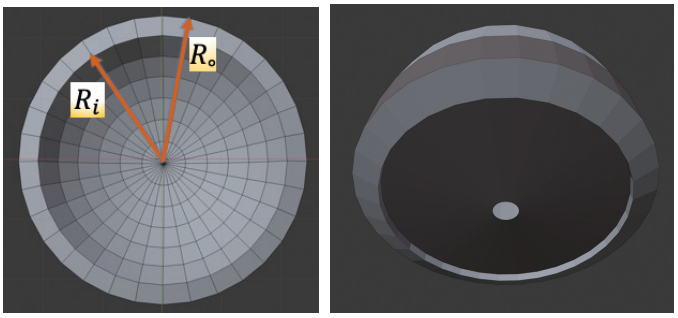

Fig. 3: **Left**: Hollow actuation chamber in in reference configuration with internal and external radii, $\{R_i, R_o\}$ illustrated. **Right**: Back cover (exterior) and side cross-section.

to exert appropriate push on an object. The robots are planar-shaped with a wall thickness of $1cm$ and diameter of $9cm$.

B. Mechanisms Setup

We now describe the mechanism of the complete motion compensation system. We propose 3 IAB kinematic chains totaling 8 IABs around the patient's H&N region as illustrated in Figure 4. The IABs have an internal cavity surrounded by two shells, which are made out of incompressible rubber materials with a Poisson's ration of approximately 0.5. For simulation purposes, the internal shell has a wall thickness of 2.5cm.

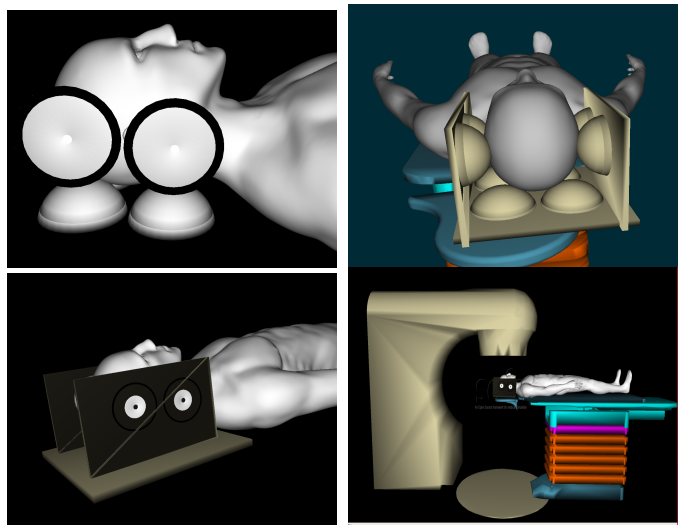

Fig. 4: System setup. **Top Left**: Side view of soft manipulators around H&N region while a patient lies in a supine position. **Top Right**: Top-down view of system setup. **Bottom Left**: Carbon nanotube IAB holder, preventing slippage of head around IABs. This system is 100% radiation transparent and typically used in H&N radiation therapy delivery. **Bottom Right**: Overall setup with gantry, turntable and couch system. [Image best visualized in colored ink].

The internal cavity ensures the hollow IAB holds the head in place. The outer shell encapsulates the inner shell such that local volume preservation is fulfilled between configuration changes. This isochoric property and the incompressibility constraints of the IAB material is important in the mathematical derivations of the mechanism's constitutive model. Each IAB in the closed kinematic chain is linked to the couch – each supporting only a part of the total load, redistributing link-loads and solving) some of the problems with serial links. uld like to have the contacting regions between the IABs and head and neck locations to have regions of their surfaces shaped into profiles that allow continuous contact along e.g. a curve or a straight line. This would enforce nonholonomic constraints as the bodies roll without slipping at the *region of contact* on one another. This way, the load that an IAB supports would be distributed over a narrow strip, essentially an atlas, rather than a localized region around a point. An engaging pair of 3D-printed teeth on spur gears would touch along a straight line; helical, hypoid or worm gears would have engaging teeth along complicated spatial curves that enforce this constraint. This constraint is important since it would allow us define the profile of the motion when the IAB exerts a motion on the head.

III. Deformation Analysis

In this section, we present the deformation analysis of the hemispherical IABs based on mechanism Type I of § II. We analyze the stress laws and constitutive relations that govern their deformation and conclude the section by solving the boundary value problem under the assumptions of *incompressibility* of the isotropic elastic IAB material and the inextensible mesh that constrains the deformation along the circumferential

directions. We present the kinematics of the IAB based on a relationship between internal pressure, Cauchy stress, stored strain energy, and the position vector of the IAB, *i.e.* (21). We make the assumption that volume does not change locally during deformation at a configuration $\chi(t)$ at time t. We work from a continuum mechanics framework, whereby we consider only final configurations of the soft robot. For a background material on this section, we refer readers to [1, §2-§3] and [27]. The commonly used notations throughout the rest of this paper is listed in Table I.

A. Nonlinear Elastic Deformation Model

As we are dealing with fluids in the chambers of the IABs, *we use the Eulerian specification in our stress field equations*. Forces that produce deformations are derived using the strain energy-invariants relationship. For readers implementing these principles on solids or hyperelastic materials, a Lagrangean formulation may be appropriate since a reference configuration may be chosen to coincide with the geometry of the solid initially.

Suppose that circular fibers (made out of non-woven fabric materials) are embedded within the elastomeric IAB volume as a reinforcement for conformal radially symmetric deformation. Further, suppose that the elastic properties of the elastomer matrix and fiber reinforcing are described in terms of the strain-energy functions Ψ_{iso} and Ψ_{mesh} respectively. Choosing a Mooney-Rivlin formulation [28], [29], we find that Ψ_{iso} depends on the elastomeric invariants I_1, and I_2 which are functions of the principal stretches, $\lambda_r, \lambda_\phi, \lambda_\theta$ *i.e.* ,

$$\begin{aligned} I_1 &= \mathbf{tr}(\mathbf{C}) = \lambda_r^2 + \lambda_\phi^2 + \lambda_\theta^2, \quad \text{and} \\ I_2 &= \mathbf{tr}(\mathbf{C}^{-1}) = \lambda_r^{-2} + \lambda_\phi^{-2} + \lambda_\theta^{-2}, \end{aligned} \tag{1}$$

where $\lambda_r\lambda_\phi\lambda_\theta = 1$ following the incompressibility assumption of the elastomeric IAB material [30]. The Mooney-Rivlin strain energy for small deformations as a function of the strain invariants of (1) is

$$\Psi_{\text{iso}}(I_1, I_2) = \frac{1}{2}C_1(I_1 - 3) + \frac{1}{2}C_2(I_2 - 3). \tag{2}$$

The fiber membrane's strain energy is constrained along the circumferential direction $\mathbf{M}$ so that it only applies along the radial, r and zenith axes, ϕ (see Figure 5$|_L$). We set the strain energy invariant as $I_4 = \mathbf{M}\cdot\mathbf{CM}$, where the symbol "$\cdot$" denotes the dot product and we choose the standard reinforcing model *i.e.* ,

$$\Psi_{\text{mesh}}(I_4) = \frac{C_4}{2}(I_4 - 1)^2 \tag{3}$$

where C_4 is the fiber stiffness. We consider the material to be incompressible ($J \equiv \det \mathbf{F} = 1$) with the total energy of the elastomer-fiber composite being

$$\Psi(I_1, I_2, I_4) = \Psi_{\text{iso}}(I_1, I_2) + \Psi_{\text{mesh}}(I_4). \tag{4}$$

To find a closed-form expression for I_4, we consider a strip of the IAB material in the XY plane with vectors $\mathbf{M}$ in the reference configuration forming circular segments with angles γ as shown in Figure 5. The matrix forms of $\mathbf{M}$ and $\mathbf{M}'$ are

$$\mathbf{M} = [\cos\gamma,\ \sin\gamma,\ 0]^T,\ \mathbf{M}' = [\cos\gamma,\ -\sin\gamma,\ 0]^T. \tag{5}$$

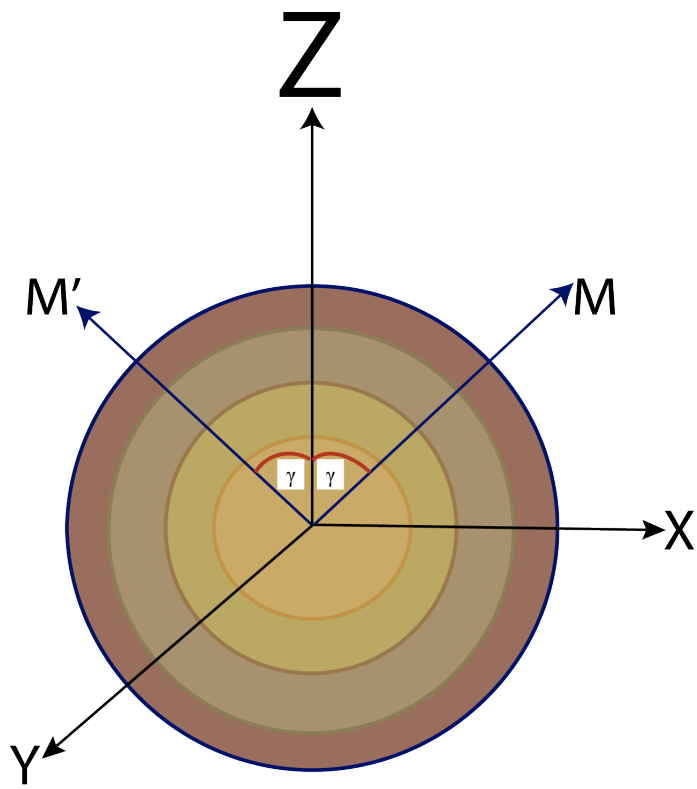

Fig. 5: Sketch of an IAB strip reinforced by circular fiber membranes radially symmetric with respect to the edges at angles, γ, along directions $\boldsymbol{M}$ and $\boldsymbol{M}'$.

The anisotropy term is only active $I_4 > 1$ so that he matrix bears the stress under compression in the fiber direction. If there is a deformation, we must have

$$\mathbf{m} = \mathbf{FM} = \begin{bmatrix} \lambda_r\cos\gamma & \lambda_\phi\sin\gamma & 0 \end{bmatrix}^T. \tag{6}$$

where λ_r and λ_ϕ are the principal stretches along the axial and zenith directions, respectively. The fiber invariant is,

$$I_4 = \mathbf{M}\cdot\mathbf{CM} = \left[\lambda_r^2\cos^2\gamma,\ \lambda_\phi^2\sin^2\gamma,\ 0\right]^T \tag{7}$$

and by symmetry we have $\mathbf{M}'\cdot\mathbf{CM}' = I_4$.

B. Strain Analysis: The Deformation Gradient

Since the physical texture of the deformed IAB material is a hemisphere we choose spherical polar coordinates (r, ϕ, θ), where r represents the radial distance of the particle from a fixed origin, θ is the azimuth angle on a reference plane through the origin and orthogonal to the polar angle, ϕ. Denote the internal and external radii as r_i, and r_o respectively with current/reference configuration constraints,

$$\begin{aligned} r_i \le r \le r_o, \quad 0 \le \theta \le 2\pi, \quad 0 \le \phi \le \pi/2 \\ R_i \le R \le R_o, \quad 0 \le \Theta \le 2\pi, \quad 0 \le \Phi \le \pi/2. \end{aligned} \tag{8}$$

The position vectors $\mathbf{R}$ and $\mathbf{r}$ in either configurations are

$$\mathbf{R} = \begin{pmatrix} R\cos\Theta\sin\Phi, \\ R\sin\Theta\sin\Phi, \\ R\cos\Phi \end{pmatrix},\ \mathbf{r} = \begin{pmatrix} r\cos\theta\sin\phi, \\ r\sin\theta\sin\phi, \\ r\cos\phi \end{pmatrix} \tag{9}$$

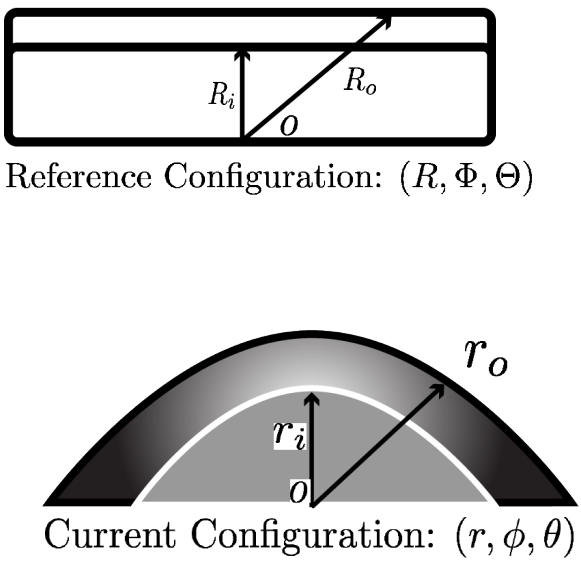

Fig. 6: Radii change under deformation.

with the material volume $\frac{2}{3}\pi\left(R^3 - R_i^3\right)$ contained between the IAB walls (of radii R_o and R_i respectively) remaining constant throughout deformation, being equal in volume to $\frac{2}{3}\pi\left(r^3 - r_i^3\right)$ so that

$$r^3 = R^3 + r_i^3 - R_i^3, \quad \theta = \Theta, \quad \phi = \Phi. \tag{10}$$

For bases $\{\boldsymbol{e}_x\}$ and $\{\boldsymbol{e}_X\}$ (with respect to an observer) in the current and reference configurations respectively, we introduce the gradient operator (in Lagrangean axes) for a fiber element $\mathbf{dx} = \mathbf{dx}_r\boldsymbol{e}_r + \mathbf{dx}_\phi\boldsymbol{e}_\phi + \mathbf{dx}_\theta\boldsymbol{e}_\theta$ (in Eulerian axes)

$$\boldsymbol{\nabla} = \boldsymbol{e}_R\frac{\partial}{\partial R} + \boldsymbol{e}_\Phi\frac{1}{R}\frac{\partial}{\partial \Phi} + \boldsymbol{e}_\Theta\frac{1}{R\sin\Phi}\frac{\partial}{\partial\Theta}. \tag{11}$$

The deformation gradient, $\mathbf{F}$, as a dyadic product of a material line element in the current configuration and the gradient operator (11) is

$$\begin{aligned}\mathbf{F} &= \mathbf{dx}\otimes\boldsymbol{\nabla}\\ &= (\mathbf{dx}_r\boldsymbol{e}_r + \mathbf{dx}_\phi\boldsymbol{e}_\phi + \mathbf{dx}_\theta\boldsymbol{e}_\theta)\otimes\\ &\left(\boldsymbol{e}_R\frac{\partial}{\partial R} + \boldsymbol{e}_\Phi\frac{1}{R}\frac{\partial}{\partial\Phi} + \boldsymbol{e}_\Theta\frac{1}{R\sin\Phi}\frac{\partial}{\partial\Theta}\right).\end{aligned} \tag{12}$$

We can verify that the following deformation gradient relation holds (using (10) as a representative fiber material)

$$\mathbf{F} = \begin{pmatrix} \frac{R^2}{r^2} & -\frac{\phi}{R} & -\frac{\theta}{R} \\ 0 & \frac{r}{R} + \frac{1}{R} & -\frac{\theta}{R}\cot\phi \\ 0 & 0 & \frac{r}{R} + \frac{\phi}{R}\cot\phi + \frac{1}{R\sin\Phi} \end{pmatrix} \tag{13}$$

(see Appendix A for the derivation). The principal stretches are given by

$$\lambda_r = \frac{R^2}{r^2};\ \lambda_\phi = \frac{r}{R} + \frac{1}{R};\ \lambda_\theta = \frac{r}{R} + \frac{\phi}{R}\cot\phi + \frac{1}{R\sin\Phi} \tag{14}$$

with the associated right and left Cauchy-Green tensors

$$\mathbf{C} = \mathbf{B} = \begin{bmatrix} \frac{R^4}{r^4} & 0 & 0 \\ 0 & \left(\frac{1}{R} + \frac{r}{R}\right)^2 & 0 \\ 0 & 0 & \left(\frac{r}{R} + \frac{\phi}{R}\cot\phi + \frac{1}{R}\csc\phi\right)^2 \end{bmatrix} \tag{15}$$

C. Macroscopic Representation of Deformation

At a material point $\mathbf{X}$ of the IAB surface in a configuration $\mathscr{B}$, it can be verified that the tensor $\mathbf{C}-\mathbf{I}$ represents a change in length of an arbitrary line element of the material. For the material not to be strained, we must have the Lagrangean strain tensor (strain rate) as zero *i.e.* $\mathbf{E} = \frac{1}{2}(\mathbf{C}-\mathbf{I}) = 0$. A particle $\mathbf{X}$'s displacement from the reference to the current configurations must be such that the point difference $d = \boldsymbol{x} - \mathbf{X}$ is $d(\mathbf{X}) = \chi(\boldsymbol{X}) - \mathbf{X}$, where $\chi(\boldsymbol{X})$ follows the notations of [1], [8], [27]. We therefore characterize the point differences by the two-point *displacement gradient*,

$$\mathbf{D} = \text{Grad } d(\mathbf{X}) = \mathbf{F} - \mathbf{I}. \tag{16}$$

For the unit vectors $\mathbf{m}$ and $\mathbf{M}$ for material line elements $\mathbf{dx}$ and $\mathbf{dX}$ in the current and reference configurations respectively[3], it follows from the invariant of deformation that

$$\mathbf{m}|\mathbf{dx}| = \mathbf{FM}|\mathbf{dX}| \implies |\mathbf{dx}|^2 = \mathbf{M}\cdot(\mathbf{CM})|\mathbf{dX}|^2. \tag{17}$$

So that the *stretch* between line elements $\mathbf{dx}$ and $\mathbf{dX}$ is

$$\lambda(\mathbf{M}) = \frac{|\mathbf{dx}|}{|\mathbf{dX}|} = |\mathbf{FM}| \equiv (\mathbf{M}\cdot(\mathbf{CM}))^{\frac{1}{2}}. \tag{18}$$

In the same vein, for line elements $\mathbf{dX}$ and $\mathbf{dX}'$ with unit tangent vectors $\mathbf{M}$ and $\mathbf{M}'$ at points $\mathbf{X}$ and $\mathbf{X}'$ in the reference configuration; these fibers correspond to $\mathbf{dx}$ and $\mathbf{dx}'$ with unit vectors $\mathbf{m}$ and $\mathbf{m}'$ at points $\mathbf{x}$ and $\mathbf{x}'$ in the current configuration. Let β denote the angle between the directions $\mathbf{M}$ and $\mathbf{M}'$ and let α be the angle between directions $\mathbf{m}$ and $\mathbf{m}'$; then

$$\mathbf{dx} = \mathbf{FdX}, \quad \mathbf{dx}' = \mathbf{FdX}', \quad \beta = \cos^{-1}(\mathbf{M}\cdot\mathbf{M}'), \tag{19a}$$

$$\text{and } \alpha = \cos^{-1}(\mathbf{m}\cdot\mathbf{m}') = \cos^{-1}(\mathbf{M}\cdot(\mathbf{CM}')/\lambda(\mathbf{M})\cdot\lambda(\mathbf{M}')). \tag{19b}$$

In the plane of shear of $\mathbf{M}$ and $\mathbf{M}'$, the *angle of shear* between the material line elements is the reduction in angles

$$\phi = \beta - \alpha. \tag{20}$$

Notice that both (16), and (18) are characterized by the stretch $\lambda = r/R$ and the radius in the current configuration (c.f. [8]). Therefore, we take the kinematic quantities that characterize the IAB deformation as

$$\mathbf{r} = \begin{bmatrix}\lambda \\ \phi\end{bmatrix} = \begin{bmatrix} r/R \\ \beta - \alpha\end{bmatrix} \tag{21}$$

i.e. $\mathbf{r}$ is a function of material stretch, and the angle of shear between material line elements.

[3] $\mathbf{d}\boldsymbol{x}$ and $\mathbf{dX}$ are respectively the material line elements at the points $\boldsymbol{x}$ and $\mathbf{X}$ in their respective configurations *i.e.* $\mathscr{B}_0$, $\mathscr{B}$.

D. Stress Response from Strain Energy

We are concerned with the magnitudes of the differential stress on the IAB shells from a mechanical point of view and *our approach is based on a continuum mechanics viewpoint which is independent of finite element methods*. Since the IAB deforms at ambient temperature, we take thermodynamic properties such as temperature and entropy to have negligible contribution. The IAB material stress response, $\mathbf{G}$, at any point on the IAB's boundary at time t determines the Cauchy stress, $\boldsymbol{\sigma}$, as well as the history of the motion up to and at the time t [27]. The *constitutive equation* that relates the stress to an arbitrary motion will be determined using [31]'s *determinism for the stress principle*. The constitutive relation for the nominal stress deformation for an elastic IAB material is given by

$$\boldsymbol{\sigma} = \begin{pmatrix} \sigma_{rr} & \sigma_{r\theta} & \sigma_{r\phi} \\ \sigma_{\phi r} & \sigma_{\phi\theta} & \sigma_{\phi\phi} \\ \sigma_{\theta r} & \sigma_{\theta\theta} & \sigma_{\theta\phi} \end{pmatrix} = \mathbf{G}(\mathbf{F}) + q\mathbf{F}\frac{\partial \boldsymbol{\Lambda}}{\partial \mathbf{F}}(\mathbf{F}), \tag{22}$$

where $\mathbf{G}$ is a functional with respect to the configuration χ, q acts as a Lagrange multiplier, and $\boldsymbol{\Lambda}$ denotes the internal (incompressibility) constraints of the IAB system. For an incompressible material, the indeterminate Lagrange multiplier becomes the hydrostatic pressure *i.e.* $q = -p$ [32]. The incompressibility of the IAB material properties imply that $\boldsymbol{\Lambda} \equiv \det \mathbf{F} - 1$. We can verify that

$$\boldsymbol{\sigma} = \mathbf{G}(\mathbf{F}) - p\mathbf{I} \tag{23}$$

following the isochoric assumption *i.e.* , $\det(\mathbf{F}) = 1$. In terms of the stored strain energy, we find that

$$\boldsymbol{\sigma} = \frac{\partial \Psi}{\partial \mathbf{F}}\mathbf{F}^T - p\mathbf{I} \tag{24}$$

where $\mathbf{I}$ is the identity tensor and p represents an arbitrary hydrostatic pressure. It follows that the constitutive law that governs the Cauchy stress tensor is

$$\begin{aligned}
\boldsymbol{\sigma} &= \frac{\partial \Psi_{\text{iso}}}{\partial \mathrm{I}_1}\frac{\partial \mathrm{I}_1}{\partial \mathbf{F}}\mathbf{F}^T + \frac{\partial \Psi_{\text{iso}}}{\partial \mathrm{I}_2}\frac{\partial \mathrm{I}_2}{\partial \mathbf{F}}\mathbf{F}^T + \frac{\partial \Psi_{\text{mesh}}}{\partial \mathrm{I}_4}\frac{\partial \mathrm{I}_4}{\partial \mathbf{F}}\mathbf{F}^T - p\mathbf{I} \\
&= \frac{1}{2}C_1\frac{\partial \mathbf{tr}\left(\mathbf{F}\mathbf{F}^T\right)}{\partial \mathbf{F}}\mathbf{F}^T + \frac{1}{2}C_2\frac{\partial \mathbf{tr}(\left[\mathbf{F}^T\,\mathbf{F}\right]^{-1})}{\partial \mathbf{F}}\mathbf{F}^T \\
&\quad + C_4(I_4 - 1)\left[\frac{\partial\left(\mathbf{M}\cdot\mathbf{C}\mathbf{M}\right)}{\partial \mathbf{F}} + \frac{\partial\left(\mathbf{M}'\cdot\mathbf{C}\mathbf{M}'\right)}{\partial \mathbf{F}}\right] - p\,\mathbf{I} \\
&= C_1\mathbf{F}\mathbf{F}^T - C_2\left(\mathbf{F}^T\mathbf{F}\right)^{-1} \\
&\quad + 2C_4(I_4 - 1)\left[(\mathbf{F}\mathbf{M})(\mathbf{F}\mathbf{M})^T + (\mathbf{F}\mathbf{M}')(\mathbf{F}\mathbf{M}')^T\right] - p\mathbf{I} \\
\boldsymbol{\sigma} &= C_1\mathbf{B} - C_2\mathbf{C}^{-1} + 2C_4(I_4 - 1)\left[\mathbf{m}\otimes\mathbf{m} + \mathbf{m}'\otimes\mathbf{m}'\right] - p\mathbf{I}.
\end{aligned} \tag{25}$$

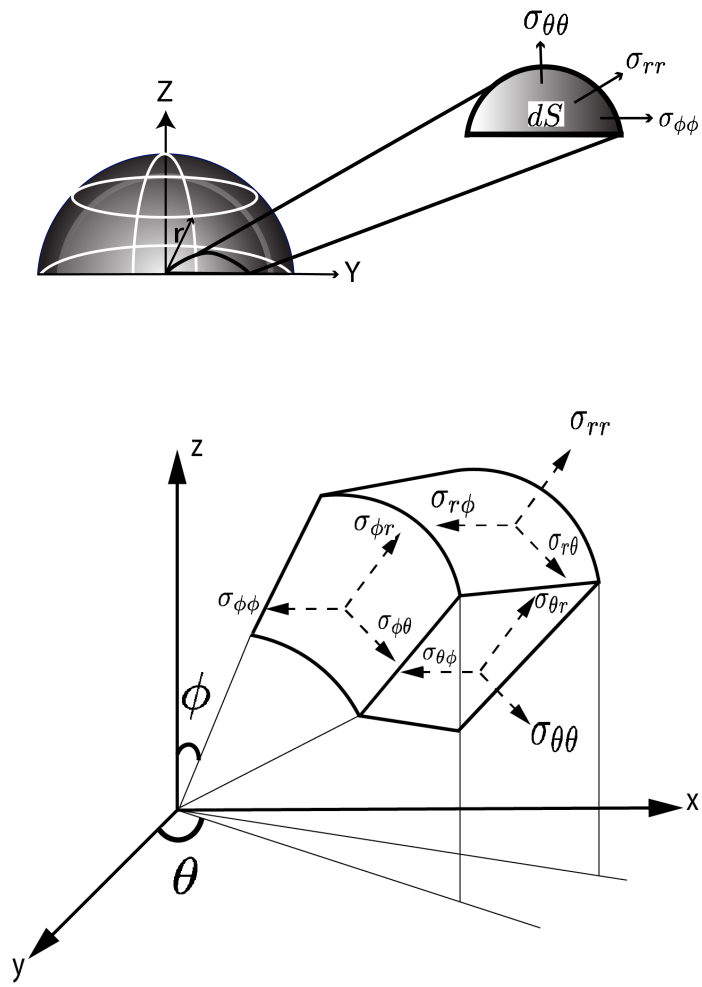

Fig. 7: Stress distribution on the IAB's differential surface, dS.

Expanding (25), we see that the shear stresses vanish so that the normal stresses are given by

$$\begin{aligned}
\sigma_{rr} &= -p + \frac{R^4}{r^4}C_1 - \frac{r^4}{R^4}C_2 - 2C_4\frac{R^8}{r^8}\cos^2\gamma \\
&\quad + 4\,C_4\frac{R^{16}}{r^{16}}\cos^4\gamma
\end{aligned} \tag{26a}$$

$$\begin{aligned}
\sigma_{\phi\phi} &= -p + \frac{(1+r)^2}{R^2}C_1 - \frac{R^2}{(1+r)^2}C_2 \\
&\quad - 2C_4(1+r)^4\sin^2\gamma\frac{\left(R^4 - 2(1+r)^4\sin^2\gamma\right)}{R^8}
\end{aligned} \tag{26b}$$

$$\begin{aligned}
\sigma_{\theta\theta} &= -p + \frac{\left(r + \phi\cot\phi + \csc\phi\right)^2}{R^2}C_1 \\
&\quad - \frac{R^2}{\left(r + \phi\cot\phi + \csc\phi\right)^2}C_2.
\end{aligned} \tag{26c}$$

Additionally, $\sigma_{\theta\theta} = 0$ owing to the circumferential constraint provided by the membrane so that only σ_{rr} and $\sigma_{\phi\phi}$ contribute to the constitutive stress law. A visualization of the component stresses of (26) on the outer shells of the IAB material is illustrated in Figure 7.

E. Boundary-Value Problem of Traction

The dynamic problem is to find the stress at every point in the robot's body subjected to external forces under suitable boundary conditions. The soft elastic materials are normally positioned around the object so that body forces are applied only along the axial direction; the fixed direction of axial loading implies that the deformation is a function of conservative forces only so that uniqueness of solution of stress field equations are preserved owing to Kirchoff's theorem [33, §7.4]. Furthermore, we assume that the applied pressure does not exceed a threshold that makes the rubber material yield to the point of buckling – thus, simplifying the solutions of the ensuing partial differential equations. The equilibrium equations for the physical component vectors of the body force, $\boldsymbol{b} = \{b_r, b_\phi, b_\theta\}$ are (see [8])

$$-b_r = \frac{1}{r^2}\frac{\partial(r^2\sigma_{rr})}{\partial r} + \frac{1}{r\sin\phi}\frac{\partial(\sin\phi\sigma_{r\phi})}{\partial\phi} + \frac{1}{r\sin\phi}\frac{\partial}{\partial\theta}\sigma_{r\theta} - \frac{1}{r}(\sigma_{\theta\theta} + \sigma_{\phi\phi}) \tag{27a}$$

$$-b_\phi = \frac{1}{r^3}\frac{\partial(r^3\sigma_{r\phi})}{\partial r} + \frac{1}{r\sin\phi}\frac{\partial(\sin\phi\sigma_{\phi\phi})}{\partial\phi} + \frac{1}{r\sin\phi}\frac{\partial(\sigma_{\theta\phi})}{\partial\theta} - \frac{\cot\phi}{r}(\sigma_{\theta\theta}) \tag{27b}$$

$$-b_\theta = \frac{1}{r^3}\frac{\partial(r^3\sigma_{\theta r})}{\partial r} + \frac{1}{r\sin^2\phi}\frac{\partial(\sin^2\phi\sigma_{\theta\phi})}{\partial\phi} + \frac{1}{r\sin\phi}\frac{\partial}{\partial\theta}\sigma_{\theta\theta}. \tag{27c}$$

Owing to the CCOARSE symmetry of the elastic IAB materials, all shearing stresses *i.e.* $\sigma_{r\theta}, \sigma_{\phi\theta}, \sigma_{r\phi}$ etc., vanish. We prescribe the following boundary conditions for the radial normal stress

$$\sigma_{rr}|_{r=r_\circ} = -P_{\text{atm}}, \quad \sigma_{rr}|_{r=r_i} = -P_{\text{atm}} - P \tag{28}$$

where P_{atm} is the atmospheric pressure and $P > 0$ is the internal pressure exerted on the internal walls of the IAB above P_{atm} *i.e.* , $P > P_{\text{atm}}$. Furthermore, we note that $\sigma_{\theta\theta} = 0$ owing to the CCOARSE circumferential constraint. Thus, (27) becomes

$$-b_r = \frac{1}{r^2}\frac{\partial(r^2\sigma_{rr})}{\partial r} - \frac{\sigma_{\phi\phi}}{r} \tag{29a}$$

$$-b_\phi = \frac{1}{r\sin\phi}\frac{\partial}{\partial\phi}(\sin\phi\sigma_{\phi\phi}), \quad -b_\theta = 0. \tag{29b}$$

Expanding (29a) and substituting (28), we can verify that

Internal Pressure and Radial Body Force

$$P = \int_{r_i}^{r_\circ} \frac{1}{r}\left(rb_r + \sigma_{\phi\phi} - 2\sigma_{rr}\right) dr \tag{30}$$

where r, and b_r are known. Under the incompressibility properties of the IAB material we have,

$$r^3 = R^3 + r_i^3 - R_i^3, \text{ and } {r_\circ}^3 = R_\circ^3 + r_i^3 - R_i^3. \tag{31}$$

Equations (30) and (31) completely determine the inverse kinematics (SOFT IK) of the IAB material: for a required IAB deformation, it determines the internal pressurization or normal Cauchy stress required.

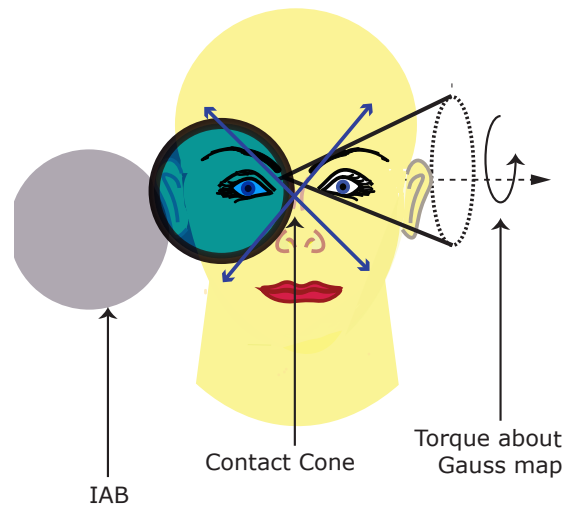

Fig. 8: Soft Contact Illustration

IV. Analysis of Contact Kinematics

The interactions among the manipulators and head are considered as a classical case of elastic bodies in contact. Using the soft finger contact primitive [34], the IAB forces and torques are modeled within a "cone of forces" about the direction of the surface normal from the object (in this case the head) (see Figure 8). The trajectory of the head under the influence of motion of an IAB is influenced by the position vector $\mathbf{r}$ of (21). When the IAB deforms, body forces in its current configuration and the *traction* over its boundary $\partial\mathcal{B}$ impact motion on the head. Constrained by the frictional coefficient, we define the soft contact force inside the friction cone as

$$\tilde{F}_{c_i} = \begin{pmatrix} \mathbf{I} & 0 \\ 0 & n_{c_i} \end{pmatrix} \begin{pmatrix} f_{c_i} \\ \tau_{c_i} \end{pmatrix}, \tag{32}$$

where $f_{c_i} \in \mathbb{R}^3$ denotes the amount of force exerted by the IAB along the direction of contact, $\tau_{c_i} \in \mathbb{R}$ is the moment of the contact force, and n_{c_i} is the *normal* or *Gauss map*[4] for a manifold $S \subset \mathbb{R}^3$ of a head surface. For contact models with friction, we require that all contact forces lie within the friction cone, determined by the frictional coefficient. The set of forces within or on the boundary of the friction cone is

$$FC = \{f_c \in \mathbb{R}^n : \|f_{c_{ij}}^t\| \leq \mu_{ij}\|f_{c_i}^n\|, \; i = 1, \ldots, k, \; j = 1, \ldots, m_i\} \tag{33}$$

where $f_{c_{ij}}^t$ is the tangent component of the jth element of the contact force, $f_{c_i}^n$ is i^{th} contact's normal force, and μ_{ij} is $f_{c_{ij}}$'s coefficient of friction.

[4]A normal map for a manifold S is a continuous map $g : S \to S^2 \subset \mathbb{R}^3$such that for every $s \in S, g(s)$ is orthogonal to S at s [35].

A. Contact/Traction Forces and Stress Equivalence

Here, we relate the microscopic contact stress of the previous section with the macroscopic descriptions of the contact friction to enable us treat different material combinations for the manipulator and head. We assume that the stress vector $\boldsymbol{\sigma}$ at a point on the IAB surface is uniform and continuous throughout the IAB boundary so that it linearly depends on the normal map (this follows from Cauchy's theorem; readers may see the proof in [27, §3.3.1]). The correspondence between material line, $\{\mathbf{dx}, \mathbf{dX}\}$, elements in the reference and current configuration is

$$\mathbf{dx} = \mathbf{F}\,\mathbf{dX} \quad \Longrightarrow \quad \mathbf{F}^{-T}\mathbf{dx} = \mathbf{dX}. \tag{34}$$

where $\mathbf{F}$ is the deformation gradient.

Let $\mathbf{H} = \mathbf{F}^{-T}$ and $\mathbf{da}$ represent an infinitesimal vector element on the material surface at a neighborhood of point $\mathbf{X}$ in $\mathscr{B}$ such that $\mathbf{da} = \mathbf{n}\mathrm{da}$, where $\mathbf{n}$ is the unit outward normal to the IAB surface. On the bounding surface of the IAB the exerted force on a surface area $\mathbf{da}$ in global form is

$$\boldsymbol{f}_c = \int_{\partial\mathscr{B}} \boldsymbol{\sigma}\,\mathbf{n}\,\mathrm{da}. \tag{35}$$

At the region of contact, we have the i'th contact force within the friction cone as

$$\begin{aligned} f_{c_i} &= (\sigma_{rr} + \sigma_{\phi\phi})\, n_{c_i} da_i \\ f_{c_i} &= \Bigg[-2p + \frac{r^4 + 2r^5 + r^6 + R^6}{r^2 R^2}\left(\frac{C_1}{r^2} - \frac{r^2}{(1+r)^2 R^2} C_2\right) \\ &\quad + 2\cos^2\gamma \frac{R^8}{r^8}\left(\cos^2\gamma \frac{R^8}{r^8} - 1\right) C_4 \\ &\quad - \frac{(1+r)^4}{R^8}\sin^4\gamma\cos(2\gamma) \\ &\quad \left(-1 - 4r - 6r^2 - 4r^3 - r^4 + 2R^4 + (1+r)^4\right) C_4\Bigg]\, n_{c_i} da_i. \end{aligned} \tag{36}$$

with the outward normal map n_{c_i} from (32). The torque is the moment of the contact force on the i'th IAB, given as

$$\tau_{c_i} = f_{c_i} \times r_{c_i} \tag{37}$$

where $r_{c_i} \in \mathbb{R}^3$ is the unit vector between the head reference point and the contact. Therefore, we have (32) as

Friction Cones' Contact Force

$$\tilde{F}_{c_i} = \begin{bmatrix} \mathbf{I} & 0 \\ 0 & n_{c_i} \end{bmatrix} \begin{bmatrix} (\sigma_{rr} + \sigma_{\phi\phi})\, n_{c_i} da_i \\ (\sigma_{rr} + \sigma_{\phi\phi})\, n_{c_i} da_i \times r_{c_i} \end{bmatrix}. \tag{38}$$

B. Contact Coordinates and Head Velocity

The head will make contact with the IAB at multiple points on its surface, so we describe the kinematics of these contact points using an atlas[5] of contact coordinate charts. In this sentiment, let C_{r_1} and C_{r_h} respectively represent a fixed reference frame with respect to the IAB and head, H (see Figure 9). Furthermore, let $S_1 \subset \mathbb{R}^3$ and $S_h \subset \mathbb{R}^3$ denote the respective *orientable manifold*[6] embeddings of the IAB and head surfaces with respect to frames C_{r_1} and C_{r_h}. We shall let S_1 and S_r belong to the *atlases* $\{S_{1_i}\}_{i=1}^{n_1}$, $\{S_{h_i}\}_{i=1}^{n_r}$ respectively. Suppose (f_1, U_1) and (f_r, U_r) are *coordinate systems* for the IAB and the head respectively, where f_i is an invertible map, $f_i(u_i, v_i) : U \to S_i \subset \mathbb{R}^3$

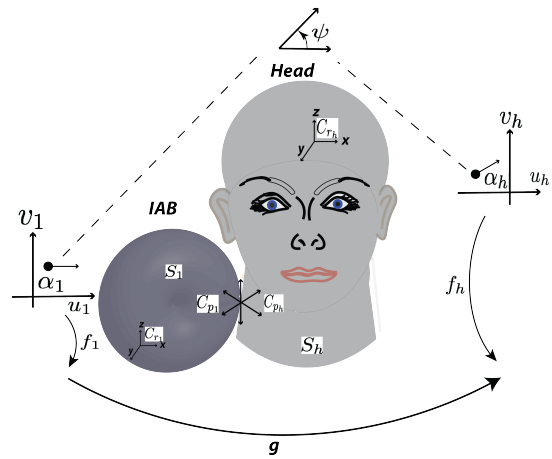

Fig. 9: Sliding and rolling contact illustration of a single IAB and the Head. [Image best visualized in colored ink].

$$f_i(u_i, v_i) : \{U \to S_i \subset \mathbb{R}^3 | i = 1, h\},$$

from an open subset U of $\mathbb{R}^2$ to a *coordinate patch* $S_i \subset \mathbb{R}^3$ such that the partial derivatives $\frac{\partial f_i}{\partial u_i}$ and $\frac{\partial f_i}{\partial v_i}$ are linearly independent. Let $p_1(t) \in S_1$ and $p_h(t) \in S_h$ represent the positions of the contact points with respect to frames C_{r_1} and C_{r_h} respectively at time t. In general, the contact points $p_1(t)$ and $p_h(t)$ will not remain in the coordinate systems S_1 and S_h for all time. Thus, we choose an interval I where $p_1(t) \in S_{1_i}$ and $p_h(t) \in S_{h_j}$ for all $t \in I$ and some i and j. As seen in Figure 9, C_{p_1} and C_{p_h} denote the contact frames that coincide with the *normalized Gauss frames* at p_1 and p_h for all $t \in I$, and α_1, α_h are local coordinate frames that describe the IAB motion with respect to the head such that

$$\alpha_1 = (u_1, v_1) \in U_1, \text{ and } \alpha_h = (u_h, v_h) \in U_h. \tag{39}$$

Let the angle between the tangent planes of α_1, and α_h be ψ. The transformation matrix $g \in \Omega \subset SE(3)$ encodes the relative orientation and position of the IAB with respect to the head where Ω is the set of all relative positions and orientations in the atlasses $\{S_{1_i}\}_{i=1}^{n_1}$, $\{S_{h_i}\}_{i=1}^{n_h}$ for which the IAB and head remain in contact. We let the *contact coordinates* be described by $\eta = (\alpha_1, \alpha_h, \psi)$. The head's motion is governed by traction forces arising from the friction tangential to the IAB surface and the pressure normal to the IAB surface. Thus, at the points

[5] An atlas $\tilde{S}$ is a set of surfaces where each surface $S \in \tilde{S}$ has an invertible map $f(\boldsymbol{u})$ from an open subset U of $\mathbb{R}^2$ to a surface $S \subset \mathbb{R}^3$ such that the partial derivatives $\frac{\partial f}{\partial u}(\boldsymbol{u})$, $\frac{\partial f}{\partial v}(\boldsymbol{v})$ are linearly independent for all $\boldsymbol{u} = (u, v) \in U$.

[6] An orientable manifold is a manifold S for which the Gauss map exists.

of contact, if $R \in SO(3)$ is the rotatory component of g, η must satisfy

$$g \circ f_1(\alpha_1) = f_h(\alpha_h) \tag{40a}$$
$$R\, n_1(\alpha_1) = -n_h(\alpha_h) \tag{40b}$$

since the contact locations must coincide for the IAB and the head, and the tangent planes must coincide so that the outward normal maps $n_1 : S_1 \to S^2 \subset \mathbb{R}^3$ and $n_h : S_h \to S^2 \subset \mathbb{R}^3$ agree. Furthermore, the orientation of the tangent planes of α_1 and α_h is the unique angle $\psi \in [0, 2\pi)$ between the x-axes of C_{p_1} and C_{p_h} such that

$$R\frac{\partial f_1}{\partial \alpha_1} M_1^{-1} R_\psi = \frac{\partial f_h}{\partial \alpha_h} M_h^{-1} \tag{41}$$

where M_i is a 2×2 square root of the Riemannian metric tensor [36] that normalizes the columns of $\frac{\partial f}{\partial \alpha}$, *i.e.*

$$M_i = \begin{bmatrix} \|\frac{\partial f_i}{\partial u_i}\| & 0 \\ 0 & \|\frac{\partial f_h}{\partial v_i}\| \end{bmatrix} \tag{42}$$

and R_ψ is chosen such that a rotation of C_{p_1} about its z-axis through $-\psi$ radians aligns the x-axes of the local coordinate system α_1 to that of the head's local coordinate system α_h *i.e.*

$$R_\psi = \begin{bmatrix} \cos\psi & -\sin\psi \\ -\sin\psi & -\cos\psi, \end{bmatrix} \tag{43}$$

with the special property that $R_\psi = R_\psi^T = R_\psi^{-1}$. We define the normalized Gauss frame at a point u on the surface U of the orthogonal coordinate system (f, U) as,

$$\begin{bmatrix} x_u & y_u & z_u \end{bmatrix} = \begin{bmatrix} \frac{\partial f}{\partial u}/\|\frac{\partial f}{\partial u}\| & \frac{\partial f}{\partial v}/\|\frac{\partial f}{\partial v}\| & n_u(f(u)) \end{bmatrix} \tag{44}$$

where x_u, y_u, and z_u are functions mapping $U \subset \mathbb{R}^2 \to \mathbb{R}^3$ and n_u is the continuous Gauss map $n_u : S \to S^2 \subset \mathbb{R}^3$. The motion of the contacts $\dot{\eta}$ as a function of components of the twist vector $\hat{\xi} = (v, w)^T$ is given in (45) as the respective *first, second*, and *third equations of contact*. Our derivation, which closely follows [37]'s multi-fingered kinematics' proof, may be found in Appendix C.

$$\dot{\alpha}_h = M_h^{-1}(\mathcal{K}_h + \tilde{\mathcal{K}}_1)^{-1}\left(\omega_t - \tilde{\mathcal{K}}_1 v_t\right) \tag{45a}$$
$$\dot{\alpha}_1 = M_1^{-1} R_\psi (\mathcal{K}_h + \tilde{\mathcal{K}}_1)^{-1}\left(\omega_t - \mathcal{K}_h v_t\right) \tag{45b}$$
$$\dot{\psi} = \omega_n + T_h M_h \dot{\alpha}_h + T_1 M_1 \dot{\alpha}_1 \tag{45c}$$

where

$$\begin{aligned}
T_h &= y_h^T \frac{\partial x_h}{\partial \alpha_h} M_h^{-1}, \quad T_1 = y_1^T \frac{\partial x_1}{\partial \alpha_1} M_1^{-1}, \\
\mathcal{K}_h &= \begin{bmatrix} x_h^T, & y_h^T \end{bmatrix}^T \frac{\partial n_h^T}{\partial \alpha_h} M_h^{-1}, \quad \omega_n = z_h^T \omega \\
\mathcal{K}_1 &= R_\psi \begin{bmatrix} x_1^T, & y_1^T \end{bmatrix}^T \frac{\partial n_1^T}{\partial \alpha_1} M_1^{-1} R_\psi, \\
\omega_t &= \begin{bmatrix} x_h^T, & y_h^T \end{bmatrix}^T \begin{bmatrix} n_h \times \omega \end{bmatrix}^T, \\
v_t &= \begin{bmatrix} x_h^T, & y_h^T \end{bmatrix}^T \begin{bmatrix} (-f_h \times \omega + v) \end{bmatrix}^T.
\end{aligned} \tag{46}$$

Note that ω_t is the rolling velocity of the head projected onto the tangent plane of the contact and v_t is the sliding velocity; ω_n is the relative rotational velocity projected to the contact's surface normal, and $\tilde{\mathcal{K}}_1 = R_\psi \mathcal{K}_1 R_\psi$ is the curvature of the IAB with respect to the contact frame that coincides with the normalized Gauss frame at $p_1(t)$. The matrix $(\mathcal{K}_h + \tilde{\mathcal{K}}_1)^{-1}$ is the so-called *relative curvature* originally coined by [35]. Simplifying (46), we find that

$$\begin{aligned}
x_h &= \frac{\partial f}{\partial u_h}/\|\frac{\partial f}{\partial u_h}\|, \quad y_h = \frac{\partial f}{\partial v_h}/\|\frac{\partial f}{\partial v_h}\|, \qquad z_h = n_u(f(u)) \\
T_h &= y_h \left[\frac{\partial x_h^T}{\partial u_h}/\|\frac{\partial f}{\partial u_h}\|, \frac{\partial x_h^T}{\partial v_h}/\|\frac{\partial f}{\partial v_h}\|\right], \\
T_1 &= y_1 \left[\frac{\partial x_1^T}{\partial u_1}/\|\frac{\partial f}{\partial u_1}\|, \frac{\partial x_1^T}{\partial v_1}/\|\frac{\partial f}{\partial v_1}\|\right], \\
\mathcal{K}_h &= \begin{bmatrix} x_h^T, & y_h^T \end{bmatrix}^T \left[\frac{\partial n_h^T}{\partial u_h}/\|\frac{\partial f}{\partial u_h}\|, \frac{\partial n_h^T}{\partial v_h}/\|\frac{\partial f}{\partial v_h}\|\right], \\
\mathcal{K}_1 &= \begin{bmatrix} x_1^T, & y_1^T \end{bmatrix}^T \left[\frac{\partial n_1^T}{\partial u_1}/\|\frac{\partial f}{\partial u_1}\|, \frac{\partial n_1^T}{\partial v_1}/\|\frac{\partial f}{\partial v_1}\|\right].
\end{aligned} \tag{47}$$

We see that for the contact interaction between an IAB and the head, for a $U \subset \mathbb{R}^2$ we must choose an appropriate $f_i : U_i \to S_i \subset \mathbb{R}^3$ in order to characterize the setup.

V. System's Newton-Euler Equations

From Truesdell's *determinism for the stress principle* [31], the Cauchy stress $\boldsymbol{\sigma}$ at any point in a material at time t for any motion up to time t determines the stress response of the material for any arbitrary motion history up to and including time t. We will derive the dynamics of the IAB system in the *strain field of the deformation*. The potential and kinetic energy of the system are considered to be derived from the constitutive strain field relations that characterize the deformation. We now use Lagrangian deformation analysis to derive the dynamic equations of the continuum multi-IAB system.

For a soft continuum body, there is an enormous amount of particle orientations during deformation; the number of particle states that is physically measurable with sensors instantaneously in a given configuration is overwhelming. However, we can leverage the constitutive law which describes the macroscopic IAB material behavior with respect to a reference frame, S, at a time, t by completely characterizing it by ten dependent variables viz., three components of the position vector, six component stress tensor variables (the shear and normal stress components), and

A. Lagrangian and Euler-Lagrange Equations

Following § III-C, we are only interested in the final position and orientation of the IAB as a whole rather than the system of particles that characterize a deformation at every time t.When the head exerts a reactive wrench on an IAB, it is natural to expect a dent. The shear angle in (21) should capture the amount of angular deformation. For a kinetic energy T and a potential energy V, the *Lagrangian,* L, of the system in generalized coordinates is the difference between the kinetic and potential energy, *i.e.*

$$L(\mathbf{r}, \dot{\mathbf{r}}) = T(\mathbf{r}, \dot{\mathbf{r}}) - V(\mathbf{r}). \tag{48}$$

The equations of motion for a pneumatic IAB system is of the form

$$\frac{d}{dt}\frac{\partial L}{\partial \dot{\mathbf{r}}_i} - \frac{\partial L}{\partial \mathbf{r}_i} = \boldsymbol{\tau}_i, \quad i = 1, \ldots, m \tag{49}$$

where $\boldsymbol{\tau}_i$ is the torque acting on the ith generalized coordinate. Written in matrix form equation, we can write the Euler-Lagrange equation of (49) as

$$\frac{d}{dt}\frac{\partial L}{\partial \dot{\mathbf{r}}} - \frac{\partial L}{\partial \mathbf{r}} = \boldsymbol{\tau}. \tag{50}$$

It now remains to derive the kinetic and potential energies for the IAB material. Let the velocity of an IAB material particle $\boldsymbol{x}$ in the current configuration at time t be $\mathbf{v}(\mathbf{r}, t)$, then the Eulerian velocity gradient tensor can be defined as

$$\boldsymbol{\Gamma} = \text{grad } \mathbf{v}(\mathbf{r}, t). \tag{51}$$

Cauchy's first law of motion [8, eq. 19] will allow us to derive the balance of mechanical energy of the system. Multiplying throughout by $\mathbf{v}$, we find that

$$\begin{aligned} \text{div } (\boldsymbol{\sigma}^T \cdot \mathbf{v}) + \rho \mathbf{b} \cdot \mathbf{v} &= \rho \mathbf{v} \cdot \dot{\mathbf{v}} \\ \text{or div } (\boldsymbol{\sigma}^T \mathbf{v}) - \mathbf{tr}(\boldsymbol{\sigma}\, \boldsymbol{\Gamma}) + \rho \mathbf{b} \cdot \mathbf{v} &= \rho \mathbf{v} \cdot \dot{\mathbf{v}}. \end{aligned} \tag{52}$$

where ρ is the IAB's mass density. Following mass conservation, we integrate over volume $\mathscr{B}$ and employ the divergence theorem, so that the above relation yields the *balance of mechanical energy*

$$\begin{aligned} \int_{\mathscr{B}} \rho \mathbf{b} \cdot \mathbf{v}\, dv + \int_{\partial \mathscr{B}} f_\rho \cdot \mathbf{v}\, da = \frac{d}{dt} \int_{\mathscr{B}} \frac{1}{2} \rho \mathbf{v} \cdot \mathbf{v}\, dv \\ + \int_{\mathscr{B}} \mathbf{tr}(\boldsymbol{\sigma}\, \boldsymbol{\Gamma})\, dv \end{aligned} \tag{53}$$

where f_ρ is the IAB body force density, and the left hand side of the foregoing is the so-called *rate of working of the applied forces*. The symmetry of the stress tensor $\boldsymbol{\sigma}$ implies that $\mathbf{tr}(\boldsymbol{\sigma}\, \boldsymbol{\Gamma}) = \mathbf{tr}(\boldsymbol{\sigma}\, \boldsymbol{\Sigma})$ where $\boldsymbol{\Sigma}$ is given in terms of the Eulerian-strain rate tensor, Γ *i.e.* ,

$$\boldsymbol{\Sigma} = \frac{1}{2}(\boldsymbol{\Gamma} + \boldsymbol{\Gamma}^T) \tag{54}$$

so that the kinetic energy density and stress power are

$$T(\mathbf{r}, \dot{\mathbf{r}}) = \frac{1}{2} \rho \mathbf{v} \cdot \mathbf{v}, \quad V(\mathbf{r}) = \mathbf{tr}(\boldsymbol{\sigma}\, \boldsymbol{\Sigma}). \tag{55}$$

B. Case I: Euler-Lagrange Equation for Cauchy-Elastic IAB Material

The stress-strain relation for the IAB we have presented are only related through the deformation tensor, implying that the material is Cauchy elastic. For Cauchy elastic materials, the stress power term is not conserved during deformation making integration over the material body $\mathscr{B}$ physically unrealistic [27]. For such materials, we may set the stored strain energy V to an arbitrary constant (e.g. $V(I) = 0$). We can derive the torque dynamics of an IAB actuator as (see proof in Appendix B)

$$\boldsymbol{\tau} = \underbrace{\begin{bmatrix} \rho/R^2 & 0 \\ 0 & \rho \end{bmatrix}}_{M_{iab}} \ddot{\mathbf{r}} + \underbrace{\begin{bmatrix} \rho \dot{r}/R^3 & 0 \\ 0 & 0 \end{bmatrix}}_{C_{iab}} \dot{\mathbf{r}}. \tag{56}$$

Rewriting equation (56) in terms of the torque for each soft robot, we have the dynamics for IAB j as

$$M_{iab_j}(\mathbf{r}_j)\ddot{\mathbf{r}}_j + C_{iab_j}(\mathbf{r}_j, \dot{\mathbf{r}}_j)\dot{\mathbf{r}}_j = \boldsymbol{\tau}_j \tag{57}$$

where M_{iab_j} and C_{iab_j} contain the respective inertia and Coriolis forces for actuator j. Since the IAB material is incompressible, the mass density is uniform throughout the body of the material. In general, we write equation (57) as

$$\boldsymbol{M}_{iab}(\tilde{\mathbf{r}})\ddot{\tilde{\mathbf{r}}} + \boldsymbol{C}_{iab}(\tilde{\mathbf{r}}, \dot{\tilde{\mathbf{r}}})\dot{\tilde{\mathbf{r}}} = \tilde{\boldsymbol{\tau}} \tag{58}$$

where $\tilde{\mathbf{r}} \in \mathbb{R}^{n_1} \times \mathbb{R}^{n_2} \times \cdots \mathbb{R}^{n_8}$ gives the generalized coordinates for all the IABs and $\tilde{\boldsymbol{\tau}}$ are the vectorized torques of the individual robots.

C. Case II: Euler-Lagrange Equation for Green Elastic IAB Material

For completeness, we treat the case where the IAB material body is *hyperelastic* (*i.e.* , *Green elastic*)[7], the eulerian form of the stress power expression is

$$V(\mathbf{r}) = \mathbf{tr}(\boldsymbol{\sigma}\, \boldsymbol{\Sigma}). \tag{59}$$

We are mostly interested in the mechanical energy in the current configuration, however, it is worthwhile to note that the equivalent relation in the Lagrangean form is

$$\begin{aligned} \int_{\mathscr{B}_\circ} \rho_\circ \mathbf{b}_\circ \dot{\boldsymbol{\chi}}\, dV + \int_{\partial \mathscr{B}_\circ} (\boldsymbol{\sigma}^T \mathbf{N}) \dot{\boldsymbol{\chi}}\, dA = \\ \frac{d}{dt} \int_{\mathscr{B}_\circ} \frac{1}{2} \rho_\circ\, \dot{\boldsymbol{\chi}} \cdot \dot{\boldsymbol{\chi}}\, dV + \int_{\mathscr{B}_\circ} \mathbf{tr}(\boldsymbol{\sigma} \dot{\mathbf{F}})\, dV, \end{aligned} \tag{60}$$

It follows that,

$$V(\mathbf{r}) = \mathbf{tr}(\boldsymbol{\sigma} \dot{\mathbf{F}}) \tag{61}$$

for a Green elastic material. Similar to the arguments in § V-B, we find the torque as (see derivation in Appendix B)

Green-Elastic IAB Material Torque

$$\begin{aligned} \boldsymbol{\tau} = \frac{\rho \ddot{r}}{R^2} + \rho \ddot{\alpha} + \frac{\rho \dot{r}^2}{R^3} + 4C_1 \left(\frac{2R^3}{r^5} + \frac{r}{R^3} \right) \\ + 4C_2 \left(\frac{2r^3}{R^5} + \frac{R}{r^3} \right). \end{aligned} \tag{62}$$

VI. Multi-IAB Statics and End-Effector Velocities

Following the CCOARSE deformation model, the regularity of the IAB in its current configuration, $\boldsymbol{\chi}(\mathbf{r}, t)$, implies that it can be uniformly defined by $\mathbf{r}$ throughout the IAB material body. Similar to [8], we are interested in the final state of the IAB after deformation; the path it takes for us to reach the final configuration is not important to us (since there is no obstacle in the continuum robots' workspace). Thus we drop the time dependence on the configuration and take $\mathbf{r}$ to be the generalized coordinate of the IAB. The configuration space of the IAB with respect to the spatial frame at a certain time can then be described by $g_{st}(\boldsymbol{\chi}) \equiv g_{st}(\mathbf{r}) : \mathbf{r} \to g_{st}(\mathbf{r}) \in SE(3)$

[7] An hyperelastic material is one where the strain-energy function exists.

while the strain state of the IAB is characterized by the strain field

$$\hat{\xi}_i(\mathbf{r}) = g_i^{-1}\frac{\partial g_i}{\partial \mathbf{r}} \in \mathfrak{se}(3) = g_i^{-1}g_i' \tag{63}$$

with the respective g_i's being the tangent vector at g_i such that $g_i' \in T_{g_i(\mathbf{r})}SE(3)$. Note that $T_{g_i(\mathbf{r})}$ is the tangent matrix at g_i with associated Lie algebra $se(3) \approx T_eSE(3)$.

A. End Effector Forces

From the derived relationship between the head contact coordinates and the relative motion (v_t, ω_t) of the IAB *i.e.* equation (45), we can associate a Jacobian that maps IAB velocities to head position and orientation. A fundamental assumption in our formulation is that the IABs make contact with the head throughout manipulation, and the manipulation is stable and prehensile. A forward kinematic map from the configuration of the $i'th$ IAB, χ_{iab_i} maps from respective IAB configurations to head position and orientation *i.e.* $K_{iab_i} : \chi_{iab_i} \to SE(3)$. The velocity of the head with respect to a fixed base frame in terms of IAB velocities can be written in terms of the forward kinematics Jacobian:

$$\begin{pmatrix} v_{iab_i} \\ \omega_{iab_i} \end{pmatrix} = \frac{\partial K_{iab_i}}{\partial \mathbf{r}_i}\frac{d\mathbf{r}}{dt}K_{iab_i}^{-1} = \boldsymbol{J}_i(\mathbf{r}_i)\dot{\mathbf{r}}_i \tag{64}$$

where $\mathbf{r}_i$ is the spatial position of IAB i, and $(v_{iab_i}^T, \omega_{iab_i}^T) \in \mathbb{R}^6$ represents the linear and angular velocity of the ith IAB about its screw basis. In essence, $\mathbf{r}_i \in \mathbb{R}^3$ with its rows of mapped to scalars by an appropriate choice of norm. The contact between the head and the IABs is mapped by the Jacobian

$$\boldsymbol{J}_{c_i}(\xi_h, \xi_{iab_i}) = \begin{bmatrix} \mathbf{I} & \hat{\boldsymbol{w}}(r_{c_i}) \\ \mathbf{0} & \mathbf{I} \end{bmatrix} J_{r_i}, \tag{65}$$

where $\boldsymbol{J}_{c_i} : \dot{\xi}_{r_i} \to \begin{bmatrix} v_{c_i}^T, & w_{c_i}^T \end{bmatrix}^T$, $r_{c_i} \in \mathbb{R}^3$ is a vector between the head reference point (e.g. the center of mass) and the contact with the ith IAB, ξ_h is the position and relative orientation of the head, ξ_{iab_i} is the position and relative orientation of the ith soft robot in world coordinates, $\hat{\boldsymbol{w}}(r_{c_i})$ is an anti-symmetric matrix for the vector r_{c_i}, and $\xi_r = (\xi_{r_1}, \xi_{r_2}, \cdots, \xi_{r_8})$ are the positions and orientations for each of the 8 IABs. The manipulation map, G_i is made up of matrices of the form

$$G_i(\xi_h, \xi_r) = \begin{bmatrix} \mathbf{I} & \mathbf{0} \\ \hat{w}(r_{c_i}) & \mathbf{I} \end{bmatrix} B_i(\xi_h, \xi_r), \tag{66}$$

where $B_i(\xi_h, \xi_r)$ is the selection map as defined in [38] for the desired manipulation. The net force on the head is a sum of the individual forces arising from each IAB. Owing to the linearity of each individual IAB's contact force, the resultant head force can be stitched together to form G, *i.e.*

$$\tilde{F}_h = \begin{bmatrix} G_1, \ldots, G_8 \end{bmatrix} \begin{pmatrix} \tilde{F}_{c_1} \\ \vdots \\ \tilde{F}_{c_8} \end{pmatrix} = G\tilde{F}_c, \tag{67}$$

where $F_h \in \mathbb{R}^6$ and $F_c \in \mathbb{R}^{m_1} \times \mathbb{R}^{m_2} \times \ldots \times \mathbb{R}^{m_8}$. The *internal* or *null forces* is captured by the null space $\mathcal{N}(G)$ of the manipulation map G; these forces correspond to zero net force on the head of the patient. Each $\tilde{F}_{c_i}$ in (67) is of the form (38).

B. End-effector Velocities

We define the velocity constraint dual of (66) as the constraint between the relative velocity of the head and that of the twist velocities of the contact point

$$\begin{pmatrix} \tilde{v}_{c_i} \\ \tilde{\omega}_{c_i} \end{pmatrix} = \begin{bmatrix} \mathbf{I} & \hat{\omega}(r_{c_i}) \\ 0 & \mathbf{I} \end{bmatrix} \begin{pmatrix} v_{c_h} \\ \omega_{c_h} \end{pmatrix}. \tag{68}$$

For a conjugate twist vector $(v_c^T, \omega_c^T)^T$ to the forces exerted by the IABs, f_c, we have the following

$$\begin{pmatrix} v_c \\ \omega_c \end{pmatrix} = G^T \begin{pmatrix} v_{c_h} \\ \omega_{c_h} \end{pmatrix}. \tag{69}$$

Given a *selection matrix* $B_i^T(\xi_h, \xi_{iab_i}) \in \mathbb{R}_i^m$ for a particular IAB, where m_i is the range of all the forces and moments for the chosen contact primitive (or union of contact primitives), the *manipulation map* for the ith IAB can be written as,

$$G_i^T(\xi_h, \xi_{iab_i})\xi_h = B_i^T(\xi_h, \xi_{iab_i})\boldsymbol{J}_{c_i}(\xi_h, \mathbf{r}_{r_i})\dot{\xi}_{iab_i} \tag{70}$$

where $\boldsymbol{J}_{c_i}$ is the contact Jacobian for the ith actuator, and ξ_h denotes the velocity of the head. For the 8 soft actuators, the manipulation constraint of the system can be written as

$$\begin{bmatrix} G_1^T \\ G_2^T \\ \vdots \\ G_8^T \end{bmatrix} \begin{pmatrix} v_h \\ w_h \end{pmatrix} = \mathbf{diag} \begin{pmatrix} B_1^T\boldsymbol{J}_{c_1} \\ B_2^T\boldsymbol{J}_{c_2} \\ \vdots \\ B_8^T\boldsymbol{J}_{c_8} \end{pmatrix} \begin{pmatrix} \dot{\mathbf{r}}_{iab_1} \\ \dot{\mathbf{r}}_{iab_2} \\ \vdots \\ \dot{\mathbf{r}}_{iab_8} \end{pmatrix}. \tag{71}$$

VII. Newton-Euler System of Equations

The dynamics of the head is a form of (58) but without the actuator torques. In local coordinates, it has the form

$$\boldsymbol{M}_h(\zeta)\ddot{\zeta} + \boldsymbol{C}_h(\zeta, \dot{\zeta})\dot{\zeta} + \boldsymbol{N}_h(\zeta, \dot{\zeta}) = 0 \tag{72}$$

with ζ being a local parameterization of the position and orientation of the head in the Lie Group $SE(3)$, and $\boldsymbol{N}_h$ being the gravitational and frictional forces exerted by/on the head. The head and the multi-DOF IAB system are connected via the manipulation constraint *i.e.*

$$G^T(\zeta, \mathbf{r})\dot{\zeta} = \boldsymbol{J}(\zeta, \mathbf{r})\dot{\mathbf{r}}. \tag{73}$$

Suppose that the velocity constraint produces a virtual displacement constraint in $\delta\zeta$ and $\delta\mathbf{r}$ such that for $q = (\zeta, \mathbf{r})$, we have

$$\delta\mathbf{r} = \boldsymbol{J}^{-1}(q)G^T(q)\delta\zeta$$

the Lagrange equations become

$$\left(\frac{d}{dt}\frac{\partial L}{\partial \dot{q}} - \frac{\partial L}{\partial q} - (\boldsymbol{\tau}, 0)\right)\delta q = 0 \tag{74a}$$

$$\begin{pmatrix} \frac{d}{dt}\frac{\partial L}{\partial \dot{\mathbf{r}}} - \frac{\partial L}{\partial \mathbf{r}} - \boldsymbol{\tau} \\ \frac{d}{dt}\frac{\partial L}{\partial \dot{\zeta}} - \frac{\partial L}{\partial \zeta} \end{pmatrix}^T \begin{pmatrix} \delta\mathbf{r} \\ \delta\zeta \end{pmatrix} = 0 \tag{74b}$$

$$\left(\frac{d}{dt}\frac{\partial L}{\partial \dot{\mathbf{r}}} - \frac{\partial L}{\partial \mathbf{r}} - \boldsymbol{\tau}\right)\delta\mathbf{r} + \left(\frac{d}{dt}\frac{\partial L}{\partial \dot{\zeta}} - \frac{\partial L}{\partial \zeta}\right)\delta\zeta = 0 \tag{74c}$$

$$GJ^{-T}\left(\frac{d}{dt}\frac{\partial L}{\partial \dot{\mathbf{r}}} - \frac{\partial L}{\partial \mathbf{r}} - \boldsymbol{\tau}\right)\delta\zeta + \left(\frac{d}{dt}\frac{\partial L}{\partial \dot{\zeta}} - \frac{\partial L}{\partial \zeta}\right)\delta\zeta = 0 \tag{74d}$$

wherefore,

$$\left(\frac{d}{dt}\frac{\partial L}{\partial \dot{\zeta}} - \frac{\partial L}{\partial \zeta}\right)\delta\zeta + GJ^{-T}\left(\frac{d}{dt}\frac{\partial L}{\partial \dot{\mathbf{r}}} - \frac{\partial L}{\partial \mathbf{r}}\right) = GJ^{-T}\boldsymbol{\tau} \tag{75}$$

given the arbitrariness of $\delta\zeta$. Equations (75) alongside (73) completely describe the system dynamics. Putting (57) into (75), we have

$$\left(\frac{d}{dt}\frac{\partial L}{\partial \dot{\zeta}} - \frac{\partial L}{\partial \zeta}\right)\delta\zeta = GJ^{-T}\left(1 - \frac{\rho}{2\|\mathbf{r}\|^2}\right)\boldsymbol{\tau}. \tag{76}$$

VIII. Results

We now describe in detail the implementation of the kinematics and dynamics of the system we have been describing so far.

A. SOFA Simulation

We rely on the SOFA simulation framework [39] to realize our vision. We compose the system's scene graph as shown in Figure 4. The patient is modeled as rigid and in contact with the soft domes. In all our interactive simulations, we separate the mechanical finite models from the collision and visual models in order to exploit distributed yet time-realistic evaluation of the various parts of our scene. The various geometric objects in the setup are hierarchically related to one another via a mapping mechanism. This mechanism propagates the forces and displacements that relate the several collisions, contacts, deformations, and displays and synchronizes them during simulation. Barycentric coordinates (t_1, t_2, t_3) [40], which are masses at the vertices of a triangle $\Delta T_1\, T_2\, T_3$, are used to map the IAB mesh models to the collision and visual models. This way, we are able to reduce the computational time spent during simulation on the collision and mechanical models.

The soft domes are modeled as solid mechanical bodies in Blender [41]. We then discretized the IAB solid models into polyhedral platonic solids using the CGAL library [42] as illustrated in Figure 10. Choosing tetrahedrons as the finite solid elements, at a facet angle of 10°, 1mm circumferential radius, and $0.1mm$ facet size for the Delaunay balls, we generate 4,784 tetrahedrons for each IAB mesh. For each tetrahedron in the mesh, we compute the spherical polar coordinate position vector using (9) using the rectangular coordinate equivalence to (9) $i.e.$

$$r^2 = x^2 + y^2 + z^2, \quad \theta = \tan^{-1}\left(\frac{y}{x}\right)$$
$$\phi = \cos^{-1}\left(\frac{z}{r}\right) \tag{77}$$

for each face of the polyhedron. We then update the associated deformation gradient $\mathbf{F}$, as well as the left and right Cauchy-Green deformation tensors $\mathbf{B}$ and $\mathbf{C}$ respectively. In all our simulations, we set r to $r_\circ$ and R to $R_\circ$. The state of the IAB is a vector which contains all its positional and velocity degrees of freedom.

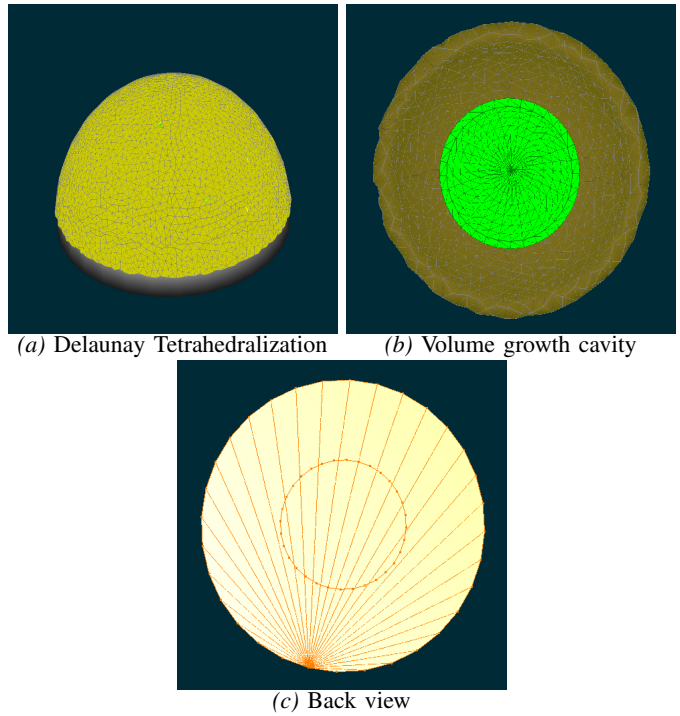

(a) Delaunay Tetrahedralization *(b)* Volume growth cavity

(c) Back view

Fig. 10: Finite Element Model of IAB Dome

IX. Conclusions

We have presented the kinematic motion equations and the Lagrangian dynamics for the mechanism presented in our previous publication. It remains to demonstrate the working examples in closed-loop head motion control. In a follow-up paper to be released shortly, we show how these formulations are applied in real-time on the patient-IAB system.

Appendix A
Deformation Gradient Derivation

It can be verified that the orthonormal basis vectors for (9) are

$$\boldsymbol{e}_r = \frac{\partial \mathbf{r}}{\partial r}/|\frac{\partial \mathbf{r}}{\partial r}| = \begin{bmatrix}\cos\theta\,\sin\phi\\ sin\theta\,\sin\phi\\ \cos\phi\end{bmatrix} \quad \boldsymbol{e}_\phi = \frac{\partial \mathbf{r}}{\partial \phi}/|\frac{\partial \mathbf{r}}{\partial \phi}| = \begin{bmatrix}\cos\theta\cos\phi\\ \sin\theta\cos\phi\\ -\sin\phi\end{bmatrix}$$
$$\boldsymbol{e}_\theta = \frac{\partial \mathbf{r}}{\partial \theta}/|\frac{\partial \mathbf{r}}{\partial \theta}| = \begin{bmatrix}-\sin\theta\\ \cos\theta\\ 0\end{bmatrix}. \tag{78}$$

From (12), we can write

$$\mathbf{F} = \frac{\partial(\mathbf{dx}_r)}{\partial R}\boldsymbol{e}_r \otimes \boldsymbol{e}_R + \frac{1}{R}\frac{\partial}{\partial \Phi}(\mathbf{dx}_r\boldsymbol{e}_r) \otimes \boldsymbol{e}_\Phi + \frac{1}{R\sin\Phi}\frac{\partial(\mathbf{dx}_r\boldsymbol{e}_r)}{\partial \Theta} \otimes \boldsymbol{e}_\Theta \tag{79a}$$
$$+ \frac{\partial}{\partial R}(\mathbf{dx}_\phi\boldsymbol{e}_\phi) \otimes \boldsymbol{e}_R + \frac{1}{R}\frac{\partial}{\partial \Phi}(\mathbf{dx}_\phi\boldsymbol{e}_\phi) \otimes \boldsymbol{e}_\Phi$$

$$
\begin{aligned}
&= \frac{\partial(\mathbf{dx}_r)}{\partial R}\boldsymbol{e}_r \otimes \boldsymbol{e}_R + \frac{1}{R\sin\Phi}\frac{\partial(\mathbf{dx}_r)}{\partial\Theta}\boldsymbol{e}_r \otimes \boldsymbol{e}_\Theta + \mathbf{dx}_r \frac{\sin\phi}{R\sin\Phi}\boldsymbol{e}_\theta \otimes \boldsymbol{e}_\Theta \\
&\quad + \frac{\mathbf{dx}_r}{R}\boldsymbol{e}_\phi \otimes \boldsymbol{e}_\Phi + \frac{1}{R}\frac{\partial(\mathbf{dx}_r)}{\partial\Phi}\boldsymbol{e}_r \otimes \boldsymbol{e}_\Phi + \frac{\partial(\mathbf{dx}_\phi)}{\partial R}\boldsymbol{e}_\phi \otimes \boldsymbol{e}_R + 0 \\
&\quad - \frac{\mathbf{dx}_\phi}{R}\boldsymbol{e}_r \otimes \boldsymbol{e}_\Phi + \frac{1}{R}\frac{\partial(\mathbf{dx}_\phi)}{\partial\Phi}\boldsymbol{e}_\phi \otimes \boldsymbol{e}_\Phi + \cos\phi\frac{\mathbf{dx}_\phi}{R\sin\Phi}\boldsymbol{e}_\theta \otimes \boldsymbol{e}_\Theta \\
&\quad + \frac{1}{R\sin\Phi}\frac{\partial(\mathbf{dx}_\phi)}{\partial\Theta}\boldsymbol{e}_\phi \otimes \boldsymbol{e}_\Theta + \frac{\partial(\mathbf{dx}_\theta)}{\partial R}\boldsymbol{e}_\theta \otimes \boldsymbol{e}_R + 0 \\
&\quad + \frac{1}{R}\frac{\partial(\mathbf{dx}_\theta)}{\partial\Phi}\boldsymbol{e}_\theta \otimes \boldsymbol{e}_\Phi + 0 + \frac{1}{R\sin\Phi}\frac{\partial(\mathbf{dx}_\theta)}{\partial\Theta}\boldsymbol{e}_\theta \otimes \boldsymbol{e}_\Theta \\
&\quad + \frac{\mathbf{dx}_\theta}{R\sin\Phi}\left(-\boldsymbol{e}_r\sin\phi - \boldsymbol{e}_\phi\cos\phi\right) \otimes \boldsymbol{e}_\Theta
\end{aligned}
\tag{79b}
$$

where we have made use of the chain rule, (10), together with the identities,

$$
\frac{\partial \boldsymbol{e}_r}{\partial r} = \frac{\partial \boldsymbol{e}_\phi}{\partial r} = \frac{\partial \boldsymbol{e}_\theta}{\partial r} = \frac{\partial \boldsymbol{e}_\theta}{\partial \phi} = 0 \quad \frac{\partial \boldsymbol{e}_\phi}{\partial \phi} = -\boldsymbol{e}_r \quad \frac{\partial \boldsymbol{e}_r}{\partial \phi} = \boldsymbol{e}_\phi \tag{80a}
$$

$$
\frac{\partial \boldsymbol{e}_r}{\partial \theta} = \boldsymbol{e}_\theta\,\sin\phi \quad \frac{\partial \boldsymbol{e}_\phi}{\partial \theta} = \boldsymbol{e}_\theta\cos\phi \quad \frac{\partial \boldsymbol{e}_\theta}{\partial \theta} = -\left(\boldsymbol{e}_r\sin\phi + \boldsymbol{e}_\phi\cos\phi\right) \tag{80b}
$$

in carrying out the partial derivatives of (79). In matrix form, we rewrite (79) as

$$
\mathbf{F} = \begin{pmatrix}
\frac{\partial(\mathbf{dx}_r)}{\partial R} & \frac{\partial(\mathbf{dx}_r)}{R\partial\Phi} - \frac{\mathbf{dx}_\phi}{R} & \frac{1}{R\sin\Phi}\frac{\partial(\mathbf{dx}_r)}{\partial\Theta} - \frac{\sin\phi}{R\sin\Phi}\mathbf{dx}_\theta \\
\frac{\partial(\mathbf{dx}_\phi)}{\partial R} & \frac{\mathbf{dx}_r}{R} + \frac{1}{R}\frac{\partial(\mathbf{dx}_\phi)}{\partial\Phi} & \frac{1}{R\sin\Phi}\frac{\partial(\mathbf{dx}_\phi)}{\partial\Theta} - \frac{\cos\phi}{R\sin\Phi}\mathbf{dx}_\theta \\
\frac{\partial(\mathbf{dx}_\theta)}{\partial R} & \frac{1}{r}\frac{\partial\,\mathbf{dx}_\theta}{\partial\phi} & \frac{1}{R\sin\Phi}\left(\frac{\partial(\mathbf{dx}_\theta)}{\partial\Theta} + \cos\phi\mathbf{dx}_\phi + \sin\phi\mathbf{dx}_r\right)
\end{pmatrix} \tag{81}
$$

which as a result of (10), becomes

$$
\mathbf{F} = \begin{pmatrix}
\frac{\partial(\mathbf{dx}_r)}{\partial R} & \frac{\partial(\mathbf{dx}_r)}{R\partial\Phi} - \frac{\mathbf{dx}_\phi}{R} & \frac{1}{R\sin\Phi}\frac{\partial(\mathbf{dx}_r)}{\partial\Theta} - \frac{\mathbf{dx}_\theta}{R} \\
\frac{\partial(\mathbf{dx}_\phi)}{\partial R} & \frac{\mathbf{dx}_r}{R} + \frac{1}{R}\frac{\partial(\mathbf{dx}_\phi)}{\partial\Phi} & \frac{1}{R\sin\Phi}\frac{\partial(\mathbf{dx}_\phi)}{\partial\Theta} - \cot\phi\frac{\mathbf{dx}_\theta}{R} \\
\frac{\partial(\mathbf{dx}_\theta)}{\partial R} & \frac{1}{r}\frac{\partial\,\mathbf{dx}_\theta}{\partial\phi} & \frac{\mathbf{dx}_\phi}{R}\cot\phi + \frac{\mathbf{dx}_r}{R} + \frac{1}{R\sin\Phi}\frac{\partial(\mathbf{dx}_\theta)}{\partial\Theta}
\end{pmatrix} \tag{82}
$$

or

$$
\mathbf{F} = \begin{pmatrix}
\frac{R^2}{r^2} & -\frac{\phi}{R} & -\frac{\theta}{R} \\
0 & \frac{r}{R} + \frac{1}{R} & -\frac{\theta}{R}\cot\phi \\
0 & 0 & \frac{r}{R} + \frac{\phi}{R}\cot\phi + \frac{1}{R\sin\Phi}
\end{pmatrix}. \tag{83}
$$

Appendix B
Robot-Head Dynamics

We now derive the overall dynamics for the elastic IAB in Eulerian form. Following (21), a point on the surface of the IAB has the following description

$$
\mathbf{r} = \begin{bmatrix}\lambda \\ \phi\end{bmatrix} = \begin{bmatrix} r/R \\ \beta - \alpha\end{bmatrix} \tag{84}
$$

so that the Eulerian time differentiation of $\mathbf{r}$ yields

$$
\dot{\mathbf{r}} = \left[\dot{\lambda}, \quad \dot{\phi}\right]^T = \left[\dot{r}/R, \quad -\dot{\alpha}\right]^T \tag{85}
$$

which follows since $\dot{R} = \dot{\beta} = 0$ in the reference configuration. Similarly, we find that $\ddot{\mathbf{r}}$ is

$$
\ddot{\mathbf{r}} = \left[\ddot{\lambda}, \quad \ddot{\phi}\right]^T = \left[\ddot{r}/R, \quad -\ddot{\alpha}\right]^T \tag{86}
$$

Recall the kinetic energy form of a continuum body (§ V)

$$
T = \frac{1}{2}\rho\mathbf{v}(\mathbf{r},t)\cdot\mathbf{v}(\mathbf{r},t) = \frac{1}{2}\rho\|\dot{\mathbf{r}}\|^2. \tag{87}
$$

Given the incompressibility of the IAB material body, the material mass density is uniform throughout the body at a configuration so that the rate of change of of the body mass, ρ, vanishes.

A. Case I: Cauchy Elastic IAB Material Skins

Suppose we choose a Cauchy Elastic material so that the constitutive equation that governs the Cauchy stress tensor, $\boldsymbol{\sigma}$, is independent of the path of the deformation from the reference configuration but is solely a function of the state of deformation. Then, it follows that $V = 0$. We have

$$
T = \frac{1}{2}\rho\|\dot{\mathbf{r}}\|^2 = \frac{1}{2}\rho\left(\dot{r}^2/R^2 + \dot{\alpha}^2\right), \; V = 0. \tag{88}
$$

It follows that the Lagrangian is

$$
L(\mathbf{r},\dot{\mathbf{r}}) = \frac{1}{2}\rho\|\dot{\mathbf{r}}\|^2 = \frac{1}{2}\rho\left(\dot{r}^2/R^2 + \dot{\alpha}^2\right) \tag{89}
$$

and the derivatives of the canonical momenta are

$$
\frac{d}{dt}\frac{\partial L}{\partial \dot{r}} = \frac{d}{dt}\left(\frac{\rho\,\dot{r}}{R^2}\right) = \rho\left(\frac{\ddot{r}}{R^2} - 2\frac{\dot{r}\dot{R}}{R^3}\right) \equiv \frac{\rho}{R^2}\ddot{r} \tag{90a}
$$

$$
\frac{d}{dt}\frac{\partial L}{\partial \dot{\phi}} = \frac{d}{dt}\frac{\partial L}{\partial \dot{\alpha}} = \frac{d}{dt}\left(\rho\dot{\alpha}\right) = \rho\ddot{\alpha}, \tag{90b}
$$

where (90a) follows from the fact that the radius is constant in the reference configuration. We therefore have the following associated generalized forces

$$
\frac{\partial L}{\partial r} = 0, \frac{\partial L}{\partial R} = -\frac{\rho\dot{r}^2}{R^3} \text{ and } \frac{\partial L}{\partial \phi} = 0. \tag{91a}
$$

Recalling the Euler-Lagrange equation from (50), we may write the torque that governs the $j'th$ IAB as (we have dropped the $j'th$ index)

Cauchy-Elastic IAB Material Torque

$$\boldsymbol{\tau} = \frac{\rho\ddot{r}}{R^2} + \rho\ddot{\alpha} + \frac{\rho\dot{r}^2}{R^3} \tag{92}$$

and in matrix form for all the system of IABs, we have

$$\boldsymbol{\tau} = \begin{bmatrix} \rho/R^2 & 0 \\ 0 & \rho \end{bmatrix} \begin{bmatrix} \ddot{r} \\ \ddot{\alpha} \end{bmatrix} + \begin{bmatrix} \dot{r} \\ \dot{\alpha} \end{bmatrix}^T \begin{bmatrix} \rho/R^3 & 0 \\ 0 & 0 \end{bmatrix} \begin{bmatrix} \dot{r} \\ \dot{\alpha} \end{bmatrix} \tag{93}$$

rewritten compactly as,

$$\boldsymbol{\tau} = \underbrace{\begin{bmatrix} \rho/R^2 & 0 \\ 0 & \rho \end{bmatrix}}_{M_{iab}} \ddot{\mathbf{r}} + \underbrace{\begin{bmatrix} \frac{\rho}{R^3}\dot{r} & 0 \\ 0 & 0 \end{bmatrix}}_{C_{iab}} \dot{\mathbf{r}} \tag{94}$$

or

$$\boldsymbol{\tau} = M_{iab}(\mathbf{r})\ddot{\mathbf{r}} + C_{iab}(\mathbf{r}, \dot{\mathbf{r}})\dot{\mathbf{r}} \tag{95}$$

B. Case II: Green Elastic IAB Material Skins

When the stress tensor depends on the strain, we have from (61), that

$$V(\mathbf{r}) = \mathbf{tr}(\boldsymbol{\sigma}\Sigma). \tag{96}$$

The associated force on the head is now a function of the kinetic and potential energies so that we have

$$L(\mathbf{r}, \dot{\mathbf{r}}) = \frac{1}{2}\rho\|\dot{\mathbf{r}}\|^2 + \mathbf{tr}(\boldsymbol{\sigma}\dot{\mathbf{F}}) \tag{97a}$$

$$= \frac{1}{2}\rho\left(\dot{r}^2/R^2 + \dot{\alpha}^2\right) + \mathbf{tr}(\boldsymbol{\sigma}\dot{\mathbf{F}}). \tag{97b}$$

We thus have

$$L(\mathbf{r}, \dot{\mathbf{r}}) = \frac{1}{2}\rho\left(\dot{r}^2/R^2 + \dot{\alpha}^2\right) + \mathbf{tr}(\boldsymbol{\sigma}\dot{\mathbf{F}}) \tag{98}$$

Solving for the derivatives of the kinetic and potential energies as before, we have

$$\frac{d}{dt}\frac{\partial L}{\partial \dot{r}} = \frac{\rho}{R^2}\ddot{r}, \; \frac{d}{dt}\frac{\partial L}{\partial \dot{\phi}} = \rho\ddot{\alpha} \tag{99a}$$

with the following associated generalized forces

$$\frac{\partial L}{\partial r} = -4C_2\left(\frac{2r^3}{R^5} - \frac{R}{r^3}\right) - 4C_1\left(\frac{2R^3}{r^5} - \frac{r}{R^3}\right), \tag{100a}$$

and $$\frac{\partial L}{\partial \phi} = 0. \tag{100b}$$

We can now write the torque as

Green-Elastic IAB Material Torque

$$\boldsymbol{\tau} = \frac{\rho\ddot{r}}{R^2} + \rho\ddot{\alpha} + \frac{\rho\dot{r}^2}{R^3} + 4C_1\left(\frac{2R^3}{r^5} + \frac{r}{R^3}\right) + 4C_2\left(\frac{2r^3}{R^5} + \frac{R}{r^3}\right) \tag{101}$$

Appendix C
Derivation of IAB-Head Contact Kinematics

Here, we formulate the contact kinematics between an IAB and the head in a fashion similar to the single finger soft contact type postulated in [37]. We note that an alternative derivation that is more concise can be found in [35].

A. Contact Coordinates and Gaussian Map

Following equations (40a), (40b), and 41, we write

$$R\,f_1(\alpha_1) + p = f_h(\alpha_h) \tag{102a}$$

$$R\,n_1(\alpha_1) = -n_h(\alpha_h) \tag{102b}$$

$$R\,\frac{\partial f_1}{\partial \alpha_1}\,M_1^{-1}\,R_\psi = \frac{\partial f_h}{\partial \alpha_h}\,M_h^{-1}. \tag{102c}$$

Differentiating (102a) and (102b), we find that

$$\dot{R}\,f_1(\alpha_1) + R\,\frac{\partial f_1}{\partial \alpha_1}\dot{\alpha}_1 + \dot{p} = \frac{\partial f_h}{\partial \alpha_h}\dot{\alpha}_h \tag{103}$$

$$\dot{R}\,n_1(\alpha_1) + R\,\frac{\partial n_1}{\partial \alpha_1}\dot{\alpha}_1 = -\frac{\partial n_h}{\partial \alpha_h}\dot{\alpha}_h. \tag{104}$$

It follows through the multiplication of (103) by $\frac{\partial f_h}{\partial \alpha_h}^T$ and putting α_h into (104), we have

$$\dot{R}\,n_1(\alpha_1) + R\,\frac{\partial n_1}{\partial \alpha_1}\dot{\alpha}_1 = -\frac{\partial n_h}{\partial \alpha_h}M_h^{-2}\frac{\partial f_h}{\partial \alpha_h}^T \left(\dot{R}\,f_1(\alpha_1) + R\,\frac{\partial f_1}{\partial \alpha_1}\dot{\alpha}_1 + \dot{p}\right). \tag{105}$$

Now, putting (102c) into (105) and rearranging, we find that

$$\left[R\,\frac{\partial n_1}{\partial \alpha_1} + \frac{\partial n_h}{\partial \alpha_h}M_h^{-2}\left(\frac{\partial f_h^T}{\partial \alpha_h}\frac{\partial f_h}{\partial \alpha_h}\right)M_h^{-1}\,R_\psi M_1\right]\dot{\alpha}_1 = -\dot{R}\,n_1 - \frac{\partial n_h}{\partial \alpha_h}M_h^{-2}\frac{\partial f_h}{\partial \alpha_h}^T\left(\dot{R}\,f_1(\alpha_1) + \dot{p}\right). \tag{106}$$

Multiplying throughout by $M_h^{-T}\frac{\partial f_h}{\partial \alpha_h}^T$, we have on the left hand side of the above as,

$$M_h^{-T}\frac{\partial f_h}{\partial \alpha_h}^T\left(R\,\frac{\partial n_1}{\partial \alpha_1} + \frac{\partial n_h}{\partial \alpha_h}M_h^{-1}\,R_\psi M_1\right)\dot{\alpha}_1. \tag{107}$$

Since

$$M_h^{-T}\frac{\partial f_h}{\partial \alpha_h}^T = \frac{\partial f_h}{\partial \alpha_h}M_h^{-1} = \left(R\,\frac{\partial f_1}{\partial \alpha_1}\,M_1^{-1}\,R_\psi\right)^T = R_\psi\,M_1^{-T}\,\frac{\partial f_1}{\partial \alpha_1}^T\,R^T, \tag{108}$$

equation (107) becomes

$$\dot{\alpha}_1\left(R_\psi\,M_1^{-T}\,\frac{\partial f_1}{\partial \alpha_1}^T\,\frac{\partial n_1}{\partial \alpha_1} + M_h^{-T}\frac{\partial f_h}{\partial \alpha_h}^T\frac{\partial n_h}{\partial \alpha_h}\,M_h^{-1}\,R_\psi M_1\right) = \left(R_\psi\,M_1^{-T}\,\frac{\partial f_1}{\partial \alpha_1}^T\,\frac{\partial n_1}{\partial \alpha_1}M_1^{-1}R_\psi + M_h^{-T}\frac{\partial f_h}{\partial \alpha_h}^T\frac{\partial n_h}{\partial \alpha_h}\,M_h^{-1}\right) \times R_\psi M_1\dot{\alpha}_1. \tag{109}$$

Setting

$$\tilde{\mathcal{K}}_1 = R_\psi\,M_1^{-T}\,\frac{\partial f_1}{\partial \alpha_1}^T\,\frac{\partial n_1}{\partial \alpha_1}M_1^{-1}R_\psi$$

and

$$\mathcal{K}_h = M_h^{-T} \frac{\partial f_h}{\partial \alpha_h}^T \frac{\partial n_h}{\partial \alpha_h} M_h^{-1},$$

it follows from (105) that

$$\left(\tilde{\mathcal{K}}_1 + \mathcal{K}_h\right) R_\psi M_1 \dot{\alpha}_1 =$$
$$M_h^{-T} \frac{\partial f_h}{\partial \alpha_h}^T \left[-\dot{R}\, n_1 - \frac{\partial n_h}{\partial \alpha_h} M_h^{-2} \frac{\partial f_h}{\partial \alpha_h}^T \left(\dot{R}\, f_1 + \dot{p}\right)\right]$$
$$= -M_h^{-T} \frac{\partial f_h}{\partial \alpha_h}^T \dot{R}\, n_1 - \mathcal{K}_h\, M_h^{-T} \frac{\partial f_h}{\partial \alpha_h}^T \left(\dot{R}\, f_1 + \dot{p}\right) \quad (110)$$

so that

$$\dot{\alpha}_1 = \left(\tilde{\mathcal{K}}_1 + \mathcal{K}_h\right)^{-1} R_\psi M_1^{-1} \times$$
$$\left[\underbrace{-M_h^{-T} \frac{\partial f_h}{\partial \alpha_h}^T \dot{R}\, n_1}_{w_t} - \mathcal{K}_h \underbrace{M_h^{-T} \frac{\partial f_h}{\partial \alpha_h}^T \left(\dot{R}\, f_1 + \dot{p}\right)}_{v_t} \right] \quad (111)$$

or

$$\dot{\alpha}_1 = \left(\tilde{\mathcal{K}}_1 + \mathcal{K}_h\right)^{-1} R_\psi M_1^{-1} (w_t - \mathcal{K}_h v_t). \quad (112)$$

Finding the generalized velocity of the head with respect to a single IAB deformation is tantamount to finding $(\hat{w}, v) = \dot{g}\, g^{-1}$. Thus,

$$\omega_t = -M_h^{-T} \frac{\partial f_h}{\partial \alpha_h}^T (\omega \times (R\, n_1)) = -M_h^{-T} \frac{\partial f_h}{\partial \alpha_h}^T (n_h \times \omega) \quad (113)$$

$$v_t = M_h^{-T} \frac{\partial f_h}{\partial \alpha_h}^T (\omega \times (R\, f_1) + \omega \times p + v) \quad (114)$$
$$= M_h^{-T} \frac{\partial f_h}{\partial \alpha_h}^T (-f_h \times \omega + v), \quad (115)$$

where ω_t is the head's rolling velocity projected onto the contact's tangent plane. The rotation normal to the surface is canceled by the cross product of ω and n_h. In the same vein, v_t is the sliding velocity between the contacts, projected onto the tangent plane. Following the above construction, we find the kinematics of the contact point of the head in local coordinates is

$$\dot{\alpha}_h = M_h^{-1} \left(\tilde{\mathcal{K}}_1 + \mathcal{K}_h\right)^{-1} (\omega_t - \tilde{\mathcal{K}}_1 v_t), \quad (116)$$

where $\left(\tilde{\mathcal{K}}_1 + \mathcal{K}_h\right)$ is the *relative curvature* [35]. It remains to solve for the relative orientation between the two local coordinates, ψ.

B. Relative Contact Orientation and Torsion Metric Tensors

In matrix form, (102b) and (102c) can be written as,

$$R \begin{bmatrix} \frac{\partial f_1}{\partial \alpha_1} M_1^{-1} & n_1(\alpha_1) \end{bmatrix} \begin{bmatrix} R_\psi & 0 \\ 0 & -1 \end{bmatrix} = \begin{bmatrix} \frac{\partial f_h}{\partial \alpha_h} M_h^{-1} & n_h(\alpha_h) \end{bmatrix}. \quad (117)$$

Following the normalized Gaussian frame defined in (44), we can rewrite the above equation as

$$R[x_1\, y_1\, z_1]\bar{R}_\psi = [x_h\, y_h\, z_h]. \quad (118)$$

The total derivative of (118) yields

$$\dot{R} \begin{bmatrix} x_1 & y_1 & z_1 \end{bmatrix} \bar{R}_\psi + R \begin{bmatrix} \dot{x}_1 & \dot{y}_1 & \dot{z}_1 \end{bmatrix} \bar{R}_\psi +$$
$$R \begin{bmatrix} x_1 & y_1 & z_1 \end{bmatrix} \begin{bmatrix} \dot{R}_\psi & 0 \\ 0 & 0 \end{bmatrix} = \begin{bmatrix} \dot{x}_h \\ \dot{y}_h \\ \dot{z}_h \end{bmatrix}^T. \quad (119)$$

Premultiplying by $y_1^T R^T$ and then postmultiplying by $\bar{R}_\psi \begin{pmatrix} 1 \\ 0 \\ 0 \end{pmatrix}$, with the knowledge that $\bar{R}_\psi \bar{R}_\psi = \mathbf{I}$, and the identity $y_1^T y_1 = 1$, we find that

$$y_1^T R^T \dot{R}[x_1\ y_1\ z_1]\bar{R}_\psi + y_1^T [\dot{x}_1,\ \dot{y}_1,\ \dot{z}_1]\bar{R}_\psi$$
$$+ (0\ 1\ 0) \begin{bmatrix} \dot{R}_\psi & 0 \\ 0 & 0 \end{bmatrix} = y_1^T R^T [\dot{x}_h\ \dot{y}_h\ \dot{z}_h] \quad (120)$$

$$y_1^T R^T \dot{R} x_1 + y_1^T \dot{x}_1 + (0\ 1\ 0) \begin{bmatrix} \dot{R}_\psi\, R_\psi & 0 \\ 0 & 0 \end{bmatrix} \begin{pmatrix} 1 \\ 0 \\ 0 \end{pmatrix}$$
$$= y_1^T R^T [\dot{x}_h\ \dot{y}_h\ \dot{z}_h]\bar{R}_\psi \begin{pmatrix} 1 \\ 0 \\ 0 \end{pmatrix} \quad (121)$$

$$y_1^T R^T \dot{R} x_1 + y_1^T \dot{x}_1 + (0 \quad 1) \begin{bmatrix} 0 & \dot{\psi} \\ -\dot{\psi} & 0 \end{bmatrix} \begin{pmatrix} 1 \\ 0 \end{pmatrix}$$
$$= y_1^T R^T [\dot{x}_h\ \dot{y}_h\ \dot{z}_h]\bar{R}_\psi \begin{pmatrix} 1 \\ 0 \\ 0 \end{pmatrix} \quad (122)$$

$$y_1^T R^T \dot{R} x_1 + y_1^T \dot{x}_1 - \dot{\psi} = y_1^T R^T [\dot{x}_h\ \dot{y}_h\ \dot{z}_h]\bar{R}_\psi \begin{pmatrix} 1 \\ 0 \\ 0 \end{pmatrix}. \quad (123)$$

From (118), we have that

$$\bar{R}_\psi^T \begin{bmatrix} x_1^T & y_1^T & z_1^T \end{bmatrix} R^T = \begin{bmatrix} x_h^T & y_h^T & z_h^T \end{bmatrix} \quad (124)$$

so that

$$\begin{bmatrix} x_1^T & y_1^T & z_1^T \end{bmatrix} R^T = \bar{R}_\psi \begin{bmatrix} x_h^T & y_h^T & z_h^T \end{bmatrix} \quad (125)$$

or

$$y_1^T R^T = (0\ 1\ 0)\, \bar{R}_\psi \begin{bmatrix} x_h^T & y_h^T & z_h^T \end{bmatrix}$$
$$= (0\ 1)\, R_\psi \begin{pmatrix} x_h^T \\ y_h^T \end{pmatrix}. \quad (126)$$

It follows from (123) that

$$\dot{\psi} = y_1^T R^T \dot{R} x_1 + y_1^T \frac{\partial x_1}{\partial \alpha_1} \dot{\alpha}_1$$
$$- (0,\ 1)\, R_\psi \begin{bmatrix} x_h^T \dot{x}_h & x_h^T \dot{y}_h \\ y_h^T \dot{x}_h & y_h^T \dot{y}_h \end{bmatrix} R_\psi \begin{pmatrix} 1 \\ 0 \end{pmatrix}. \quad (127)$$

Using the identities,

$$x_i^T y_i = 0, \implies \dot{x}_i^T y_i = -x_i^T \dot{y}_i = y_i^T \dot{x}_i \quad (128)$$
$$x_i^T x_i = 1, \implies \dot{x}_i^T x_i = 0, \quad (129)$$

we can rewrite (127) as

$$\dot{\psi} = y_1^T\, R^T \dot{R}\, x_1 + y_h^T \frac{\partial x_h}{\partial \alpha_h} \dot{\alpha}_h + y_1^T \frac{\partial x_1}{\partial \alpha_1} \dot{\alpha}_1$$
$$= \omega_n + T_h\, M_h\, \dot{\alpha}_h + T_1\, M_1 \dot{\alpha}_1 \quad (130)$$

where

$$\omega_n = y_1^T\, R^T\, \dot{R} x_1 = (R\, y_1)^T\, w \times (R x_1)$$
$$= (R\, z_1)^T\, \omega = z_h^T\, \omega \tag{131}$$
$$T_h = y_h \frac{\partial x_h^T}{\partial \alpha_h} M_h^{-T}, \qquad T_1 = y_1 \frac{\partial x_1^T}{\partial \alpha_1} M_1^{-T}. \tag{132}$$

It follows that the first, second and third equations of contact are given by (112), (116), and (130) respectively, *i.e.*

Equations of Contact

$$\dot{\alpha}_1 = \left(\tilde{\mathcal{K}}_1 + \mathcal{K}_h\right)^{-1} R_\psi M_1^{-1} (\omega_t - \mathcal{K}_h v_t) \tag{133a}$$
$$\dot{\alpha}_h = M_h^{-1} \left(\tilde{\mathcal{K}}_1 + \mathcal{K}_h\right)^{-1} (\omega_t - \tilde{\mathcal{K}}_1 v_t) \tag{133b}$$
$$\dot{\psi} = \omega_n + T_h\, M_h\, \dot{\alpha}_h + T_1\, M_1 \dot{\alpha}_1. \tag{133c}$$

D Acknowledgment

The author would like to thank Erik Pearson for kindly providing the CAD models of the couch and gantry used in our SOFA simulation. A vote of thanks to Ariella Mansfield for pointing out faculty with relevant expertise at Penn Engineering. In particular, the authors would like to thank Professors James Pikul and Michelle Johnson at Penn Mechanical Engineering for insightful discussions.

References

[1] O. P. Ogunmolu, "A Multi-DOF Soft Robot Mechanism for Patient Motion Correction and Beam Orientation Selection in Cancer Radiation Therapy." Ph.D. dissertation, The University of Texas at Dallas; UT Southwestern Medical Center, 2019. 1, 2, 4, 5

[2] J. M. Bern, K.-H. Chang, and S. Coros, "Interactive design of animated plushies," *ACM Transactions on Graphics (TOG)*, vol. 36, no. 4, p. 80, 2017. 1

[3] J. M. Bern, G. Kumagai, and S. Coros, "Fabrication, modeling, and control of plush robots," in *2017 IEEE/RSJ International Conference on Intelligent Robots and Systems (IROS)*. IEEE, 2017, pp. 3739–3746. 1

[4] T. Liu, S. Bouaziz, and L. Kavan, "Quasi-newton methods for real-time simulation of hyperelastic materials," *ACM Transactions on Graphics (TOG)*, vol. 36, no. 3, p. 23, 2017. 1

[5] S. Bouaziz, S. Martin, T. Liu, L. Kavan, and M. Pauly, "Projective dynamics: fusing constraint projections for fast simulation," *ACM Transactions on Graphics (TOG)*, vol. 33, no. 4, p. 154, 2014. 1

[6] U.S. Department of Health and Human Services, National Institutes of Health, National Cancer Institute. (2019) Cancer Stat Facts: Cancer of Any Site. [Online]. Available: https://seer.cancer.gov/statfacts/html/all.html 1

[7] M. D. Michaelson, S. E. Cotter, P. C. Gargollo, A. L. Zietman, D. M. Dahl, and M. R. Smith, "Management of complications of prostate cancer treatment," *CA: a cancer journal for clinicians*, vol. 58, no. 4, pp. 196–213, 2008. 1

[8] O. Ogunmolu, X. Liu, N. Gans, and R. Wiersma, "Mechanism and Constitutive Model of a Continuum Robot for Head and Neck Cancer Radiotherapy," in *IEEE International Conference on Robotics and Automation (ICRA), Paris, France*, 2020. 1, 5, 7, 10

[9] M. Giorelli, F. Renda, M. Calisti, A. Arienti, G. Ferri, and C. Laschi, "Neural Network And Jacobian Method For Solving The Inverse Statics Of A Cable-driven Soft Arm With Nonconstant Curvature," *IEEE Transactions on Robotics*, vol. 31, no. 4, pp. 823–834, 2015. 1

[10] O. Ogunmolu, A. Kulkarni, Y. Tadesse, X. Gu, S. Jiang, and N. Gans, "Soft-NeuroAdapt: A 3-DOF Neuro-Adaptive Patient Pose Correction System for Frameless and Maskless Cancer Radiotherapy," in *IEEE/RSJ International Conference on Intelligent Robots and Systems (IROS), Vancouver, BC, CA*. IEEE, 2017, pp. 3661–3668. 1, 2

[11] H. Mochiyama, "Hyper-flexible robotic manipulators," in *IEEE International Symposium on Micro-NanoMechatronics and Human Science, 2005*. IEEE, 2005, pp. 41–46. 1

[12] G. S. Chirikjian and J. W. Burdick, "The kinematics of hyper-redundant robot locomotion," *IEEE transactions on robotics and automation*, vol. 11, no. 6, pp. 781–793, 1995. 1

[13] F. Renda and L. Seneviratne, "A Geometric and Unified Approach for Modeling Soft-Rigid Multi-body Systems with Lumped and Distributed Degrees of Freedom," *2018 IEEE International Conference on Robotics and Automation (ICRA)*, pp. 1567 – 1574, 2018. 1

[14] H. Demirkoparan and T. J. Pence, "Swelling of an Internally Pressurized Nonlinearly Elastic Tube with Fiber Reinforcing," *International journal of solids and structures*, vol. 44, no. 11-12, pp. 4009–4029, 2007. 1

[15] A. Sedal, D. Bruder, J. Bishop-Moser, R. Vasudevan, and S. Kota, "A continuum model for fiber-reinforced soft robot actuators," *Journal of Mechanisms and Robotics*, vol. 10, no. 2, p. 024501, 2018. 1

[16] T. George Thuruthel, Y. Ansari, E. Falotico, and C. Laschi, "Control Strategies for Soft Robotic Manipulators: A Survey," *Soft Robotics*, vol. 5, no. 2, pp. 149–163, 2018. 1

[17] K. H. Hunt, *Kinematic Geometry of Mechanisms*. Oxford University Press, 1977. 2

[18] O. Ogunmolu, N. Gans, S. Jiang, and X. Gu, "An Image-Guided Soft Robotic Patient Positioning System for Maskless Head And Neck Cancer Radiotherapy: A Proof of Concept Study," *Medical Physics: The International Journal of Medical Physics Research and Practice*, vol. 42, pp. 3266–3266, June 2015. 2

[19] O. P. Ogunmolu, X. Gu, S. Jiang, and N. R. Gans, "A Real-Time, Soft Robotic Patient Positioning System for Maskless Head and Neck Cancer Radiotherapy: An Initial Investigation," in *Automation Science and Engineering (CASE), 2015 IEEE International Conference on, Gothenburg, Sweden*. IEEE, 2015, pp. 1539–1545. 2

[20] O. P. Ogunmolu, X. Gu, S. Jiang, and N. R. Gans, "Vision-based Control of a Soft Robot for Maskless Head and Neck Cancer Radiotherapy," in *Automation Science and Engineering (CASE), 2016 IEEE International Conference on, Fort Worth, Texas*. IEEE, 2016, pp. 180–187. 2

[21] O. Ogunmolu and R. D. Wiersma, *Towards Real-Time Motion Compensation in Radio-Transparent Robotic Radiation Therapy.* 2

[22] J. J. Allen, L. M. Mäthger, A. Barbosa, and R. T. Hanlon, "Cuttlefish use visual cues to control three-dimensional skin papillae for camouflage," *Journal of Comparative Physiology A*, vol. 195, no. 6, pp. 547–555, 2009. 2

[23] J. Pikul, I. Cohen, and R. Shepherd, "Stretchable surfaces with programmable texture," May 2 2019, uS Patent App. 16/161,029. 2

[24] J. H. Pikul, S. Li, H. Bai, R. T. Hanlon, I. Cohen, and R. F. Shepherd, "Stretchable surfaces with programmable 3d texture morphing for synthetic camouflaging skins," *Science*, vol. 358, no. 6360, pp. 210–214, 2017. [Online]. Available: https://science.sciencemag.org/content/358/6360/210 2

[25] R. T. Hanlon and J. B. Messenger, "Adaptive coloration in young cuttlefish (sepia officinalis l.): the morphology and development of body patterns and their relation to behaviour," *Philosophical Transactions of the Royal Society of London. B, Biological Sciences*, vol. 320, no. 1200, pp. 437–487, 1988. 2

[26] E. Donlon, S. Dong, M. Liu, J. Li, E. Adelson, and A. Rodriguez, "Gelslim: A high-resolution, compact, robust, and calibrated tactile-sensing finger," in *2018 IEEE/RSJ International Conference on Intelligent Robots and Systems (IROS)*. IEEE, 2018, pp. 1927–1934. 2

[27] R. Ogden, *Non-linear Elastic Deformations*. Mineola, New York: Dover Publicationbs, Inc., 1997. 4, 5, 6, 8, 10

[28] R. S. Rivlin and D. W. Saunders, "Large Elastic Deformations of Isotropic Materials. VII. Experiments on the Deformation of Rubber," *Philosophical Transactions of the Royal Society A: Mathematical, Physical and Engineering Sciences*, vol. 243, no. 865, pp. 251–288, 1950. 4

[29] M. Mooney, "A theory of large elastic deformation," *Journal of applied physics*, vol. 11, no. 9, pp. 582–592, 1940. 4

[30] L. R. G. Treloar, *The physics of rubber elasticity*. Oxford University Press, USA, 1975. 4

[31] C. Truesdell and W. Noll, *The Non-Linear Field Theories of Mechanics*. Springer, 1965. 6, 9

[32] G. A. Holzapfel, T. C. Gasser, and R. W. Ogden, "A new constitutive framework for arterial wall mechanics and a comparative study of material models," *Journal of elasticity and the physical science of solids*, vol. 61, no. 1-3, pp. 1–48, 2000. 6

[33] Y. Fung, P. Tong, and X. Chen, *Classical and computational solid mechanics*. World Scientific Publishing Company, 2001, vol. 2. 7

[34] V.-D. Nguyen, "Constructing force-closure grasps," *The International Journal of Robotics Research*, vol. 7, no. 3, pp. 3–16, 1988. 7

[35] D. J. Montana, "The Kinematics of Contact And Grasp," *The International Journal of Robotics Research*, vol. 7, no. 3, pp. 17–32, 1988. 7, 9, 14, 15

[36] M. Spivak, "A Comprehensive Introduction to Differential Geometry. Vol. V. Berkeley: Publish or Perish," *Inc. XI*, 1979. 9

[37] R. M. Murray and S. Sastry, "Grasping and Manipulation using Multi-fingered Robot Hands." in *Proceedings of Symposia in Applied Mathematics*, vol. 41, 1990, pp. 329–335. 9, 14

[38] J. R. Kerr, "An Analysis of Multi-Fingered Hands," *International Journal of Robotics Research*, no. Dept. of Mechanical Engineering, pp. 3–17, 1984. 11

[39] F. Faure, C. Duriez, H. Delingette, J. Allard, B. Gilles, S. Marchesseau, H. Talbot, H. Courtecuisse, G. Bousquet, I. Peterlik, and S. Cotin, "SOFA: A Multi-Model Framework for Interactive Physical Simulation," in *Soft Tissue Biomechanical Modeling for Computer Assisted Surgery*, ser. Studies in Mechanobiology, Tissue Engineering and Biomaterials, Y. Payan, Ed. Springer, June 2012, vol. 11, pp. 283–321. 12

[40] E. W. Weisstein, "Barycentric coordinates," 2003. 12

[41] Blender Online Community, *Blender - a 3D modelling and rendering package*, Blender Foundation, Blender Institute, Amsterdam, Available: http://www.blender.org 12

[42] The CGAL Project, *CGAL User and Reference Manual*, 5.0.1 ed. CGAL Editorial Board, 2020. [Online]. Available: https://doc.cgal.org/5.0.1/Manual/packages.html 12